Quantum Electronics **44** (7) 614–632 (2014)

INVITED PAPER

PACS numbers: 42.62.Be; 87.50.U–
DOI: 10.1070/QE2014v044n07ABEH015565

Characteristic responses of biological and nanoscale systems in the terahertz frequency range

A.A. Angeluts, A.V. Balakin, M.G. Evdokimov, M.N. Esaulkov, M.M. Nazarov, I.A. Ozheredov, D.A. Sapozhnikov, P.M. Solyankin, O.P. Cherkasova, A.P. Shkurinov

Contents

Abstract. **This paper briefly examines methods for the generation of pulsed terahertz radiation and principles of pulsed terahertz spectroscopy, an advanced informative method for studies of complex biological and nanostructured systems. Some of its practical applications are described. Using a number of steroid hormones as examples, we demonstrate that terahertz spectroscopy in combination with molecular dynamics methods and computer simulation allows one to gain information about the structure of molecules in crystals. A 'terahertz colour vision' method is proposed for analysis of pulsed terahertz signals reflected from biological tissues and it is shown that this method can be effectively used to analyse the properties of biological tissues and for early skin cancer diagnosis.**

Keywords: *terahertz radiation, biological tissue, molecular crystal, colour vision.*

A.A. Angeluts, A.V. Balakin, M.G. Evdokimov, I.A. Ozheredov, D.A. Sapozhnikov, P.M. Solyankin, A.P. Shkurinov Department of Physics, M.V. Lomonosov Moscow State University, Vorob'evy gory, 119991 Moscow, Russia; International Laser Center, M.V. Lomonosov Moscow State University, Vorob'evy gory, 119991 Moscow, Russia; e-mail: ashkurinov@gmail.com;
M.N. Esaulkov, M.M. Nazarov Institute on Laser and Information Technologies, Russian Academy of Sciences, Svyatoozerskaya ul. 1, 140700 Shatura, Moscow region, Russia;
O.P. Cherkasova Institute of Laser Physics, Siberian Branch, Russian Academy of Sciences, prosp. Akad. Lavrent'eva 13/3, 630090 Novosibirsk, Russia

Received 26 May 2014
Kvantovaya Elektronika **44** (7) 614–632 (2014)
Translated by O.M. Tsarev

1. Introduction

More than two centuries have passed since electromagnetic radiation that is now known as terahertz (THz) radiation was for the first time demonstrated experimentally, investigated and described, but there is still no clear-cut definition of the boundaries of the THz frequency range. First, such radiation was referred to as both far-IR radiation and submillimetre waves. Though sometimes 'stretched' to 30 μm [1], this range is usually defined as 0.1–1.0 mm in terms of wavelengths and is commonly included in the optical frequency range. The THz range overlaps the far-IR in the high-frequency region and the microwave range in the low-frequency region. This uncertainty is due in part to the history of this area of optics: the THz range was initially thought of as a 'narrowing' and 'redefinition' of the IR spectral region. The first mention of 'thermal rays', which include THz radiation, can be found in Magia naturalis (Natural Magic) [2], a work published as early as 1558 by Giambattista della Porta, one of the first European researchers. He was the first to show in his work that 'warm' and 'cold' can be focused by a concave mirror. Almost a hundred years after the pioneering work of Hershel [3], who analysed solar radiation in 1800 and made the first quantitative measurements of heating parameters in the visible and near-IR spectral regions, Rubens and Snow [4] studied in 1893 what is currently referred to as far-IR waves. At present, it is Rubens's work that is commonly thought of as the beginning of the 'optical' THz era. He carried out the first studies aimed at obtaining radiation in the 'high-frequency' part of the THz range (wavelengths from 30 to 300 μm) and proposed the first applications of this radiation, including gas spectroscopy.

Practical application of radiation in the 'low-frequency' part of the THz range was initiated by Bose's work [5]: using Hertz's approach to electromagnetic radiation generation, he designed pilot microwave devices and utilised them to investigate the effect of radiation near the low-frequency boundary of the THz range on biological systems [6].

The history of advances in the generation of short electromagnetic waves is tightly connected with the Maxwell Laboratory of Electromagnetism, Moscow State University, where Glagolewa-Arkadiewa continued in the 1920s P.N. Lebedev's studies aimed at the generation of short electromagnetic waves. Under Prof. Arkad'ev's guidance, she began to seek a new approach for obtaining electromagnetic radiation with wavelengths in the range between the radiowave and optical spectral regions [7].

Bridging the existing gap was of great importance for demonstrating that electromagnetic and light waves have a common nature. In 1922, Glagolewa-Arkadiewa invented a source of such waves, which she called a 'mass radiator', and presented her results on the properties of electromagnetic waves in the wavelength range 50–82 μm, between the radiowave and optical spectral regions, at a meeting of the Russian Association of Physicists in Nizhnii Novgorod [8]. The use of this source gave impetus to experimental studies in various fields, including biology [9].

Looking back at the more than hundred year history of the generation, detection and application of THz radiation, we see that the salient feature of this area of optics in recent years has been the application of THz radiation in biology and medicine. Given that THz frequencies typically coincide with the frequencies of rotational and vibrational transitions in organic molecules, THz radiation can be used for the spectral identification of molecules. This allows one to utilise THz technologies as a supplement to spectroscopic techniques based on the use of electromagnetic waves from other frequency ranges. Since the energy of THz photons is insufficient to ionise molecules in biological systems, THz spectroscopy appears to be an ideal tool for research in biology and medicine. Because of the difficulties related to the specifics of such objects, biomedical applications are among the medium- and long-term objectives of THz research.

In this paper, we discuss the basic principles underlying the use of THz radiation in biological and medical applications and nanotechnologies. First, we address specific issues pertaining to the THz range and review possible THz methods of resolving them. Next, we present several examples of how THz technologies are employed in spectroscopy. Finally, we discuss the application of THz waves in medical diagnosis. Most of the methods considered in this paper are still at the feasibility assessment stage, which is characteristic of the development of THz applications on the whole. Moreover, biological and medical studies are a relatively new application area of THz technologies, so much effort will be required for THz methods to be effectively used in this field.

2. Terahertz pulse generation and detection: general methods and techniques

The term 'terahertz spectroscopy' in its current meaning emerged in connection with the development of techniques for the generation and detection of pulsed THz radiation [10]. Coherent THz radiation is generated and detected using femtosecond laser pulses, and one measures the instantaneous electric field amplitude $E(t)$ of a THz pulse [11, 12] of ~1 ps duration. The shape of the temporal profile of the alternating electric field allows one to gain information about both the amplitude and phase of the THz radiation in a wide spectral range (from tenths of a terahertz to several terahertz) [13].

Figure 1 shows a block diagram of a pulsed THz spectrometer, which indicates its key components. A part of a femtosecond laser beam is used to excite and generate THz pulses, whose duration is determined by both the pulse generation technique and the femtosecond pulse duration. The rest of the laser beam is used in THz signal detection. The optical delay line ensures a controlled time delay between pump pulses of the generator and detector. Modulation of the THz radiation is necessary for synchronous detection of the THz radiation. The temporal resolution of the spectrometer is determined by the THz pulse duration and delay time measurement accuracy. A spectral analysis of THz signals is carried out after the temporal profile $E(t)$ is Fourier transformed into its spectral representation $E(f)$.

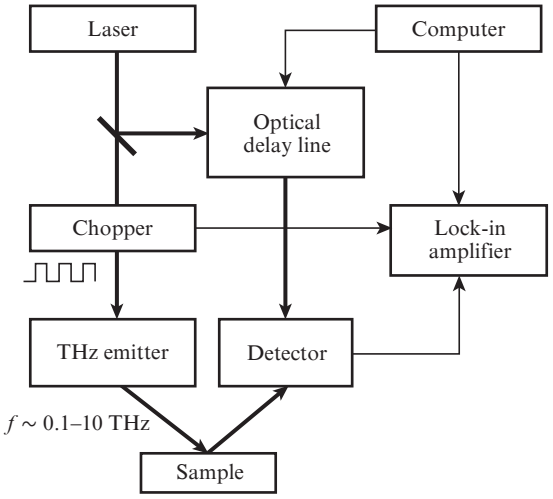

Figure 1. Block diagram of a THz spectrometer.

The methods most widely used in THz spectrometers to generate and detect THz radiation were described in detail elsewhere [14] and include conversion in a photoconductive antenna [11, 12], nonlinear optical difference frequency generation [12, 15] and the generation of THz radiation in an optical breakdown plasma [16]. All these methods have their own advantages and drawbacks, but the most commercially viable approach is to utilise photoconductive antennas, because they enable one to produce compact integrated devices. Photoconductive antennas are used not only to generate but also to detect THz pulses.

There are several approaches for realising terahertz time-domain spectroscopy (THz-TDS), which have different application fields. The measurement schemes used in THZ-TDS can be divided into two groups (Fig. 2): schemes for measuring and analysing THz radiation transmitted through an object of interest and those for measuring and analysing THz radiation reflected from the surface of an object. In a number of applications, use is made of the scheme represented on the

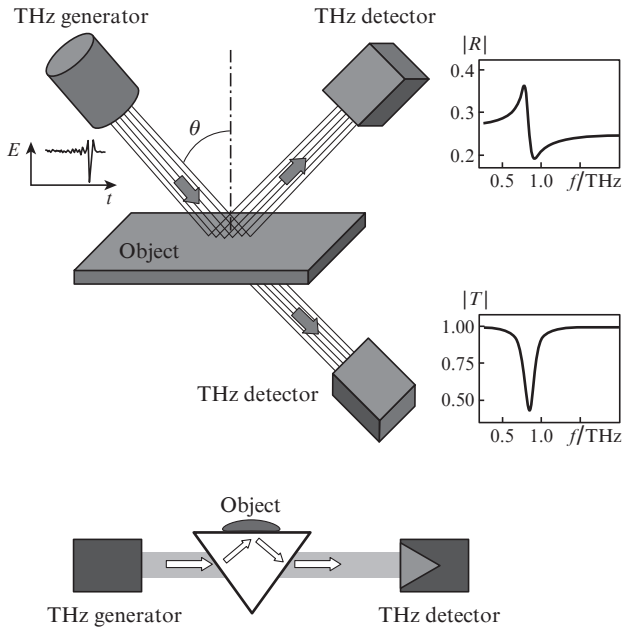

Figure 2. Measurement schemes in THz spectroscopy.

bottom of Fig. 2, which takes advantage of attenuated total reflection (ATR).

In the schemes of the former group, one measures the complex transmission coefficient of a sample: $T(f) = E_{sig}(f)/E_0(f)$, where $E_{sig}(f)$ and $E_0(f)$ are the spectra of the transmitted and incident radiation and f is linear frequency. As shown earlier [17], there is a unique relation between the measured complex transmission coefficient $T(f)$ of a substance and its parameters:

$$\alpha(f) = -\frac{\ln|T(f)| - \ln(1 - R_{av}^2)}{d},$$
$$n(f) = -\arg T(f)\frac{c}{2\pi f d} + 1, \tag{1}$$

where $\alpha(f)$ is the absorption coefficient of the substance for the THz radiation; $n(f)$ is its refractive index; d is the sample thickness; c is the speed of light; $R_{av} = (n_{av} - 1)/(n_{av} + 1)$ is the spectrum-averaged reflection coefficient; and n_{av} is the average refractive index. The last term in the first equation in (1) takes into account the reflection loss on the sample surface. In the case of a weak absorption, formulas (1) can be corrected to take into account reflections from the sample surface.

The use of a THz reflection spectrometer [12], i.e. a spectrometer configuration in which THz radiation reflected from the sample surface is analysed, makes it possible to obviate the limitations of conventional schemes for measuring transmission spectra. One such limitation is that one cannot study optically dense samples or samples on opaque substrates. Resonances seen in transmission spectra show up as well in reflection spectra. This is illustrated in Fig. 2 by the example of the transmission and reflection spectra of a particular substance. In addition, the reflection scheme makes it possible to perform remote measurements, in particular through an obstacle transparent to THz radiation, which is of most interest for practical applications.

The complex reflection coefficient can be found as the ratio of the spectra of incident and reflected radiation: $R(f) = E_{sig}(f)/E_0(f)$. For example, when a p-polarised probe beam is incident on the surface of a sample at angle θ, the reflection coefficient $R_p(f)$ is related to the complex refractive index $n^*(f)$ by a formula derived from Fresnel's formulas (see Ref. [17] for more details):

$$R_p = \frac{[n^*(f)]^2\cos\theta - \sqrt{[n^*(f)]^2 - \sin^2\theta}}{[n^*(f)]^2\cos\theta + \sqrt{[n^*(f)]^2 - \sin^2\theta}}. \tag{2}$$

Here, the complex refractive index has the form

$$n^*(f) = n'(f) + in''(f) = n(f) + i\frac{\alpha(f)\lambda}{4\pi}, \tag{3}$$

where λ is the radiation wavelength.

Solving Eqn (2) for the refractive index, we obtain

$$[n^*(f)]^2 = \varepsilon(f) = \frac{1 \pm \sqrt{1 - 4B^2\sin^2\theta}}{2B^2}, \tag{4}$$

where $B = [(1 - R_p)/(1 + R_p)]\cos\theta$ is a complex quantity and the sign of the root is determined by the physical meaning of the refractive index. From relations (3) and (4), one can obtain expressions for n and α, similar to (1), but they are too cumbersome to present them here.

Soft biological tissues and liquid samples can be characterised using THz ATR spectroscopy, in which a probe beam is refracted from a denser medium to a less dense one at an above-critical angle. The most convenient means of achieving this is a prism from a material whose refractive index exceeds that of the sample, which allows one to monitor the field penetration depth δ in the medium under study. For the interface between the medium and the prism material, we have

$$\delta = \frac{1}{(\omega/c)\sqrt{n_{12}^2\sin^2\theta - 1}}, \tag{5}$$

where ω is the frequency of the electromagnetic wave and n_{12} is the ratio of the refractive index of the prism material (n_{pr}) to that of the substance.

A prism is placed in a parallel THz beam in a pulsed THz spectrometer, as shown in Fig. 2. The radiation reflected from the clean prism base is used as a reference signal, and one measures the signal obtained when the substance of interest is pressed against the prism base (or liquid is applied to the prism base). The main advantage of ATR spectroscopy over reflection spectroscopy is that the reference spectrum (with no substance) is easy to measure. Moreover, the amplitude of the reflection coefficient in the case of ATR is near unity. The principal difficulty in ATR spectroscopy comes from the incomplete optical contact in studies of solid samples. Estimates suggest that even an air layer just 10 μm in thickness is critical because the reflection spectrum will then contain little or no information about the substance under study.

In the case of liquid samples, there is good optical contact and no such problem arises. Fresnel's formulas describing a reflection spectrum are applicable to ATR as well, but n should be replaced by n/n_{pr}. Switching from the scheme for measuring the reflection spectrum of a free surface to the scheme with a prism leads to qualitative changes in the shape of the spectra of the phase and amplitude of the reflection coefficient. Since ATR spectroscopy offers high sensitivity in a surface tissue layer no more than 10 μm thick, skin is only probed to the thickness of the horny layer. The water content of this layer is as low as 15%, and the protein and lipid contents are 70% and 15%, respectively [18]. Because of this, the reflection spectrum of skin differs significantly from that of water.

2.1. Temporal dynamics of spectral lines studied by THz spectrochronography

An approach widely used at present to analyse results of measurements of the field of a THz pulse is to measure the temporal profile of the field of a THz pulse and then convert it to the frequency domain using Fourier transformation. This allows one to gain information only about the relative amplitudes of the spectral components of the THz pulse, but not about their temporal dynamics, i.e. it remains unknown when the components emerge and how their amplitude varies with time. Fourier transforming not an entire $E(t)$ time sample but only the data in a $t_n \pm \Delta t/2$ time interval at time t_n, one can obtain an analogue of an 'instantaneous' spectrum of the signal. Shifting the time gate along the signal and repeating the procedure, one can obtain a set of 'instantaneous' spectra of the signal at different instants in time, and this set will reflect the dynamics of the spectrum of the THz pulse. Such an approach was used by Safonov et al. [19] to investigate instantaneous spectral intensities of a femtosecond pulse in time. Developing this transformation technique for analysis of the temporal profile of a THz pulse transmitted through an absorbing medium, one can obtain information about the interaction of the THz pulse with the medium in both the frequency and time domains [20].

The main idea of the gating method is to analyse the THz signal $S(t_n, t)$ resulting from the multiplication of the starting time sample by the gating function $W_n(t)$ (Fig. 3):

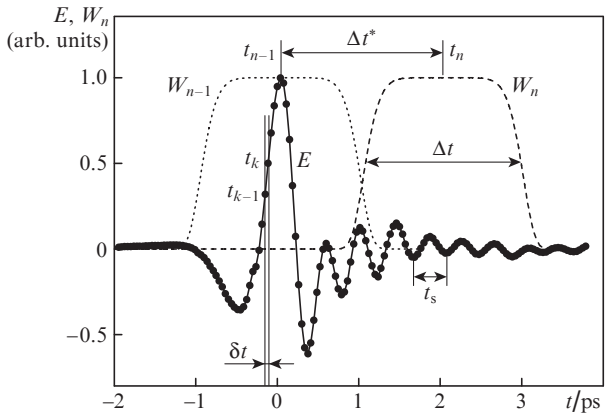

Figure 3. Field $E(t)$ of a THz signal and gating function $W_n(t)$ vs. time delay between generating and detecting laser pulses at $\Delta t = 2$ ps, $m = 4$ and $\Delta t^* = \Delta t = 2$ ps.

$$S(t_n, t) = E(t) W_n(t), \tag{6}$$

$$W_n(t) = \exp\left[-\left(\frac{t - t_n}{\Delta t}\right)^{2m}\right], \tag{7}$$

where m is a positive number characterising the slope of the edges of the gating function. Note that $W_n(t) \approx 1$ for t in the range $\Delta t_n = t_n \pm \Delta t/2$ and $W_n(t) \approx 0$ for other t values.

The field $E(t)$ of a THz pulse is measured at time intervals δt in the range $t = 0, ..., t_0$: $E_k = E(t_k)$, $t_k = k\delta t$, $k = 0, ..., N$. Thus, in going from a continuous to a discrete time dependence, the signal takes the form $S_{nk} = E_k W_n(k\delta t)$. This transformation at $m = 1$ is known as a Fourier–Gabor transformation, characterised by minimum distortions in the spectral representation of the signal because a Gaussian gating function is used. The spectrum of the signal in the time gate has the form

$$S(t_n, f) = \int_{-\infty}^{\infty} S(t_n, t) \exp(-i2\pi f t)\, dt \propto E(f) \otimes W_n(f), \tag{8}$$

where $E(f)$ and $W_n(f)$ are the $E(t)$ and $W_n(t)$ spectra, respectively. The $S(t_n, f)$ spectrum is the convolution of the spectrum of the total sample of the field of the THz pulse, $E(f)$, with the gating function spectrum, $W_n(f)$. The spectrum is calculated for all t_n values while the centre of the gate is displaced by a fixed time, Δt^*. To analyse the dynamics of a spectral component at a particular frequency, f_0, $S(t_n, f)$ is calculated at $f = f_0$.

It should be emphasised that the choice of transformation parameters – gate width Δt and gate displacement step Δt^* – is critical to this algorithm. Note that Δt^* is of the same order as Δt, and $\Delta t > 4t_s$, where $t_s = 1/f_0$ is determined by the frequency under consideration. At a smaller gate width (Δt), the result is highly dependent on the phase of the signal in the gate, which has no physical meaning. When the dynamics of two lines having similar frequencies (f_1 and f_2) are examined, it is important to take into account that, in accordance with the properties of Fourier transforms, the gate width should meet the constraint $\Delta t/2 > (f_1 - f_2)^{-1}$. Otherwise, the lines will overlap in the frequency domain and the dynamics of one line will influence that of the other. To obtain a clear picture of the dynamics of a line, the total signal detection time $t_0 = N\delta t$ should exceed at least five gate widths: $t_0 > 5\Delta t$. The δt step for obtaining a time sample can be found from the Nyquist theorem: $\delta t < 2/f_0$, where f_0 is the frequency under study. The parameter m influences both the temporal and spectral resolutions: as m increases (the gating function approaches a rectangular shape), the temporal resolution improves, but the spectral resolution becomes poorer (because the spectrum of the time gate is then described by the function $\mathrm{sinc}\, x = (\sin x)/x$, where $x = 2\pi f \Delta t/2$). In contrast, the spectrum of the $m = 1$ gating function has a Gaussian shape, $\exp[-(2\pi f)^2(\Delta t)^2/4]$, which produces minimum distortions in the frequency domain, but because the gating function also has a Gaussian shape this inevitably impairs the temporal resolution.

As an example, consider the dynamics of THz pulse absorption in L-cystine. This substance is very well suited for demonstrating the potentialities of windowed Fourier transformation because it has a sufficiently strong, isolated absorption line. The radiation–substance interaction can be considered linear because the intensity of the field of a THz pulse

in the experiment was ~1 W cm^{-2}. To obtain a theoretical fit for the absorption line, we use the classical Lorentz model, in which the complex dielectric permittivity of a medium can be represented in the form

$$\varepsilon(\omega) = \varepsilon_0 + \frac{N_e e^2}{m} \frac{1}{\omega_0^2 - \omega^2 + i\omega\Gamma}, \quad (9)$$

where e and m are the electron charge and mass; N_e is the electron concentration; ω_0 is the oscillator eigenfrequency; and Γ characterises vibration damping. The absorption coefficient $\alpha(\omega) \propto \mathrm{Im}\sqrt{\varepsilon(\omega)}$. To bring the model closer to experimental conditions, the line in question is taken to have a nonresonant background represented by a linear function of frequency (Fig. 4b). As a field acting on the medium, we use an experimentally measured field $E(t)$ of a THz pulse (Fig. 4a). In simulation, we used the parameters $\Gamma = 0.02$ ps^{-1} and $\omega_0/2\pi = 0.715$ THz, corresponding to a physical experiment.

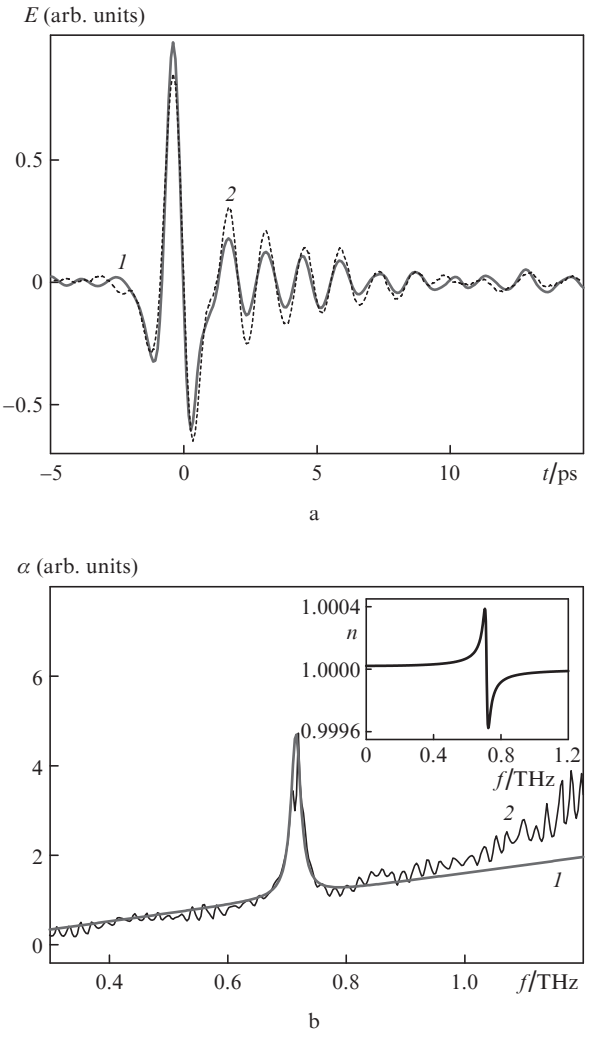

Figure 4. (*1*) Theoretically calculated and (*2*) experimentally measured (a) time-dependent field of a THz pulse transmitted through L-cystine and (b) absorption spectra of L-cystine. Inset: refractive index as a function of frequency.

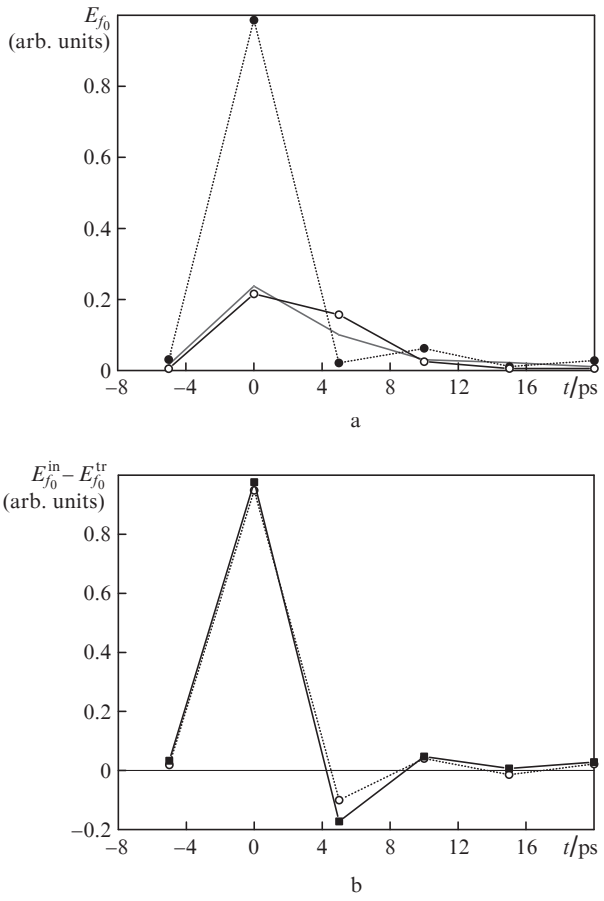

Figure 5. (a) Dynamics of spectral amplitudes (at the frequency of the 0.715-THz absorption line) for excitation (●), transmitted (○) and theoretically calculated transmitted (solid curve) pulses; (b) experimental (○) and simulated (■) dynamics of absorption in the substance.

Comparison of the theoretically calculated field of the transmitted pulse and the experimentally determined one (Fig. 4a) demonstrates that a characteristic feature of the transmitted pulse is the presence of damped harmonic oscillations due to the absorption line of the substance at a frequency of 0.715 THz. The slight discrepancy between the simulated and experimental curves is caused by the fact that the absorption line of the substance has a non-Lorentzian shape.

Consider the temporal dynamics of spectral components at a resonance frequency of 0.715 THz for incident $[E_{f_0}^{in}(t)]$ and transmitted $[E_{f_0}^{tr}(t)]$ pulses using windowed Fourier transformation (Fig. 5a) and a function of their difference $E_{f_0}^{in}(t) - E_{f_0}^{tr}(t)$ (Fig. 5b). When the difference is positive, the process will be referred to as absorption; otherwise, it will be referred to as emission. The behaviour of the function $E_{f_0}^{in}(t) - E_{f_0}^{tr}(t)$ will be referred to as the dynamics of absorption. It is seen in Fig. 5 that an incident pulse is absorbed in 3 ps, which corresponds to its duration. Next, the absorption becomes negative, i.e. the substance begins to emit (t = 3–10 ps) at the resonance frequency. In this process, the characteristic emission pulse duration τ_{rad} is of the same order as the inverse of the full width at half maximum (Γ) of the absorption line: $\tau_{rad} \approx 1/\Gamma$.

The gating function had a hyper-Gaussian shape ($m = 2$) and the temporal resolution was $\Delta t = 5$ ps. This time gate width Δt was chosen because at lower Δt values the dynamics

of absorption at the frequency in question was influenced by those in neighbouring lines of L-cystine. The time gate was displaced at time intervals $\Delta t^* = 5$ ps, equal to the gate width Δt. Simulation results for the dynamics of the same quantities are also presented in Fig. 5.

2.2. Carrier dynamics in semiconductor materials studied by an optical pump/THz probe technique

Pump–probe measurements are widely used to gain insight into the dynamics of various characteristics and properties of substances. Using this approach in THz spectroscopy, one can monitor the time variation of THz absorption spectra after optical excitation of the substance. For example, this approach is widely used to assess the temporal dynamics of the photoisomerisation of complex molecules. Of particular interest are pump–probe studies of semiconductor structures because such studies provide information about the relaxation of photoexcited carriers in semiconductors and allow one to draw conclusions as to some properties of the semiconductor that influence the temporal dynamics of photoexcited carriers.

Experiments aimed at assessing the temporal dynamics of photoexcited carriers with the possibility to cool semiconductor samples provide more detailed information about the influence of lattice defects on the properties of the semiconductor, because the transmission of a sample is determined by its electrical conductivity, which depends not only on the concentration of photoexcited carriers but also on their mobility, which in turn depends on the temperature of the semiconductor. At high temperatures, carrier scattering by the thermal vibrations of atoms in the crystal lattice (phonons) prevails, reducing the carrier mobility. At low temperatures, a key role is played by carrier scattering by defects, which leads to carrier localisation and reduced carrier mobility, so experimental studies of this effect would be expected to provide additional information about the properties of the semiconductor that influence the temporal dynamics of charge carriers.

Figure 6 shows time dependences of the maximum amplitude of a THz pulse transmitted through a gallium arsenide plate with a low-temperature layer (LT-GaAs) whose surface was exposed to laser pulses at a wavelength of 796 nm. At a negative time delay, when a pump pulse is incident on the sample surface after a THz pulse, optical pumping has no effect: the THz pulse propagates through the sample in the same way as without a pump pulse. In the case of a positive time delay, when a pump pulse arrives at the sample surface before a THz pulse, the amplitude of the transmitted THz pulse depends on the time delay because of the electron–hole pair recombination and the associated decrease in the concentration of photoexcited carriers, which in turn leads to changes in electrical conductivity. Comparison of the room-temperature and 15-K data in Fig. 6 clearly demonstrates that, at low temperatures, the photoexcited carriers relax more rapidly, suggesting that the LT gallium arsenide layer contains a high defect density.

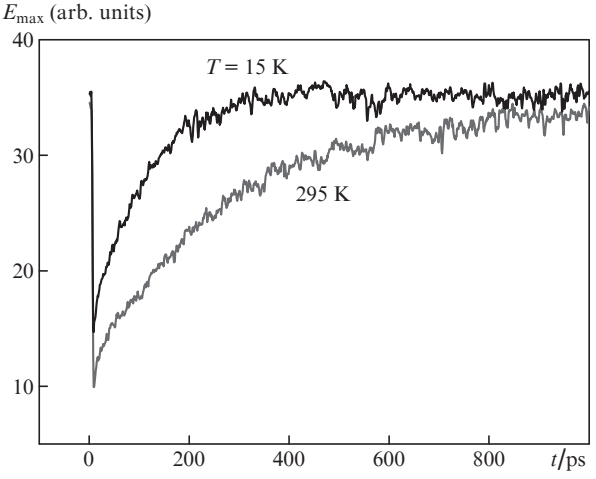

Figure 6. Maximum amplitude of a THz pulse as a function of time delay at different temperatures.

3. Spectroscopy of biological molecules, fluids and tissues

Advances in pulsed THz spectroscopy open up new possibilities in medical and biological research. This type of spectroscopy allows one to cover a wide frequency range in one measurement and obtain information about both the refractive index and absorption coefficient of the sample, thereby ensuring a complete, rapid characterisation of the substance under study. In contrast to that in the near-IR spectral region, which contains the characteristic frequencies of localised vibrations of individual chemical bonds in molecules, the spectral response of molecular systems in the THz range carries information about molecular motions of molecules as a whole: their rotations and phonon vibrations of the crystal lattice of molecular crystals [21]. The THz frequency range contains the eigenfrequencies of vibrational transitions in water molecules and key biological molecules (including nucleic acids and proteins) and intermolecular interaction frequencies. THz spectroscopy is used to gain insight into the dynamics of the formation of spatial structures in biopolymers, examine the effect of hydration on such processes [22] and assess the contribution of various noncovalent interactions to the functioning and structure of biomolecules [23]. In this section, we analyse the use of THz spectroscopy in studies of biological objects differing in complexity: molecular crystals, high molecular weight biopolymers such as DNA and proteins, biomolecule solutions, blood components and biological tissues.

3.1. Experimental studies of molecules by THz time-domain spectroscopy

In molecular crystals, which have a 'long-range' order in the arrangement of their molecules, linked by noncovalent intermolecular bonds, the excitation of phonon vibrations increases the amplitude of those intramolecular vibrations that are correlated with crystal lattice vibrations. As a result, spectra of molecular crystals in the THz frequency range contain strong absorption bands characteristic of a particular substance [24]. The THz response of molecules organised into molecular crystals to an external electromagnetic field is governed by both intra- and intermolecular interactions [25]. As a consequence, their spectra in this frequency range are highly informative and difficult to interpret.

Several approaches are used to study distinctive features of the response of molecular crystals in the THz frequency range. One of them is to produce targeted changes in the vibrational properties of molecular systems in a predeter-

mined frequency range by incorporating various heterocycles and new molecular bonds into their molecular structure. Producing such chemical bonds and changing the weight of the end groups of molecules offer the possibility of blocking some types of molecular vibrations or tuning their frequency. Comparison of quantum-mechanical calculation results and measured vibrational spectra of such molecular structures allows one to assign experimentally observed features in their THz absorption spectra to various types of intramolecular motions, which show up along with intermolecular and phonon vibrations. We applied such an approach to a series of merocyanine dyes having various end groups and π-conjugated chain lengths and showed that their THz absorption spectra were sensitive to targeted changes in the structure of their molecules: replacement of end methyl substituents by phenyl groups and an increase in conjugated chain length. We observed a clear correspondence between absorption lines in the THz frequency range and specific types of molecular vibrations: libronic vibrations of the benzene ring in the backbone of the chromophore and in the donor–acceptor end group and bending vibrations localised at the nitrogen or carbon atoms in the open polymethine chain of the dyes [24]. Their THz absorption spectra were analysed at room temperature.

Additional information about both intramolecular vibrations and intermolecular interactions in a substance can be obtained by analysing its THz absorption spectra measured at different temperatures, because changes in the temperature of a substance are accompanied by changes in its THz absorption spectrum. In many instances, the position of absorption lines in the spectrum of a substance is observed to change. This can be accounted for by the linear variation of vibrational frequencies ν with temperature T [26]:

$$\nu(T) = \nu_0(1 - \gamma_G \chi T), \tag{10}$$

where χ is the volume expansion coefficient and γ_G is the Grüneisen parameter. The intensity of absorption bands varies with temperature. The reason for this is that the distribution of molecules over vibrational levels follows the Boltzmann distribution, and cooling from room temperature to 10 K produces significant changes in the population of these levels.

Figure 7 illustrates the effect of temperature on the THz absorption spectra of L-cystine and cyclotrimethylenetrinitroamine (RDX). These results demonstrate all possible changes in absorption spectra in response to temperature changes. The example of RDX (Fig. 7b) clearly shows that the absorption peaks shift to higher frequencies with decreasing temperature, in full accord with (10). In addition, the width of the lines decreases with decreasing temperature, which is attributable to the decrease in the thermal motion of atoms, responsible for the homogeneous broadening of the lines. In the case of L-cystine (Fig. 7a), the position of its absorption lines remains essentially unchanged: we observe only that the lines become narrower and the background decreases. Note, however, that absorption lines do not always shift to higher frequencies with decreasing temperature. For example, Smirnova et al. [25] and Walther et al. [27] observed an anomalous shift of an absorption line to lower frequencies with decreasing temperature (see Fig. 9). All these facts indicate that analysis of the temperature effect on the absorption spectra of substances is a rather informative approach for gaining new data on the structure of substances, but the interpretation of results continues to be a challenging problem, which should obviously be solved by comparing experimental data to numerical simulation results, as was done in studies of the temperature effect on absorption spectra of steroid hormones [25].

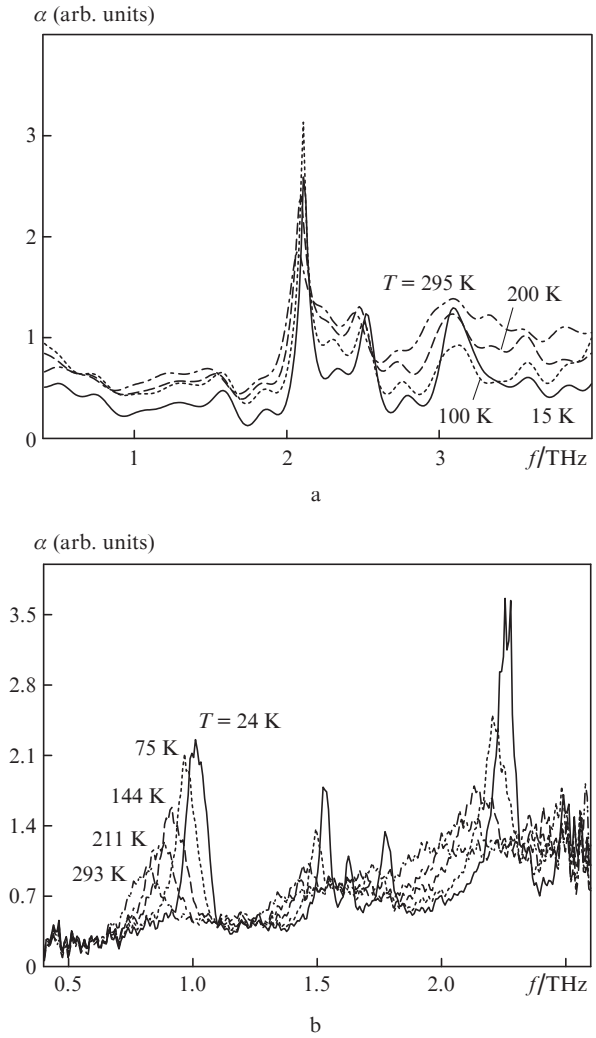

Figure 7. Effect of temperature on the absorption spectra of (a) L-cystine and (b) RDX.

Steroid hormones are an extremely important class of natural bioactive compounds that are synthesised in adrenal glands and regulate all processes in the human body and animals. According to their chemical structure, all the natural steroid hormones are cyclopentanophenanthrene derivatives and have the form of a system of four condensed rings with different substituents (Fig. 8). Such molecular systems typically possess high conformational mobility, and this shows up as low-frequency vibrations, which play a significant part in hormone receptor binding and, eventually, in the biological functions of these substances [28, 29]. The study of natural molecular systems connected by a sequence of successive biochemical transformations and differing by the presence or absence of intermolecular hydrogen bonding is another approach to understanding specific features of the response of molecular crystals in the THz frequency range [30].

The steroid hormones represented in Fig. 8 form molecular crystals with the same orthorhombic symmetry $P2_12_12_1$. Their unit cells have the form of rectangular parallelepipeds, with four molecules per cell [25, 30]. The fact that all the

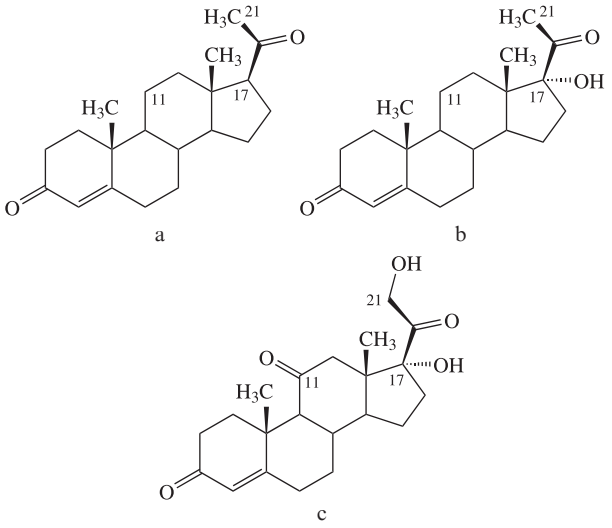

Figure 8. Structure of steroid hormones: (a) progesterone, (b) 17α-hydroxyprogesterone, (c) cortisone.

molecular systems in question are similar in spatial structure means that they are similar in long-range crystalline order, suggesting that it has a minimum effect on THz absorption spectra in going from one substance to another. The hormones in question are similar in chemical structure and differ little in molecular mass, but the number and nature of intermolecular bonds vary from molecule to molecule. The use of quantum-chemical calculations and the study of the temperature effect on absorption spectra made it possible to analyse possible vibrational species, including those involving intermolecular hydrogen bonds [25], and separately assess the contributions of molecular and phonon modes. The molecules in a molecular crystal are in general linked by van der Waals forces, which are rather weak. Hydrogen bonds are considerably stronger, which tells on molecular mobility. It is the absence of such bonds that accounts for the high mobility of the molecules and their relative independence of each other in progesterone crystals. In 17α-hydroxyprogesterone crystals, there is one hydrogen bond between the molecules, which reduces the frequency range of translational vibrations and shifts the twisting modes to lower frequencies. In cortisone crystals, there are two intermolecular hydrogen bonds, so the molecules cannot move relative to each other in parallel planes (translational motions), and even at comparatively low frequencies all the molecules are linked so tightly that any rotational motion causes twisting of their structure. Therefore, the presence of intermolecular hydrogen bonds would be expected to shift certain absorption lines in measured vibrational spectra to lower frequencies.

The main results of the studies in question demonstrate that steroid crystals free of hydrogen bonds experience high-Q vibrations, the lines in their THz absorption spectra are rather narrow for molecular crystals (progesterone), and their position varies with temperature by 2 to 6 cm^{-1}, depending on the line (Fig. 9). The presence of a hydroxyl group and, hence, the presence of an intermolecular hydrogen bond in a steroid molecule lead to damping of some types of motion, considerably broaden its lines and reduce the total number of lines. The position of the lines varies insignificantly with temperature. It has been shown that the total energy of all the

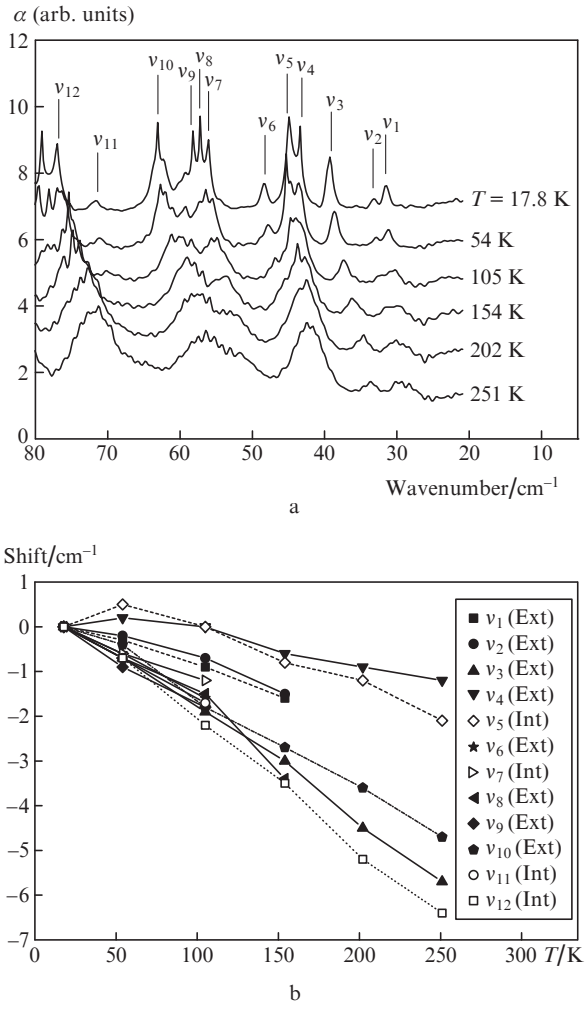

Figure 9. Effect of temperature on (a) the THz absorption spectrum of progesterone and (b) peak positions in the spectrum; Ext = external vibrations (of the crystal lattice as a whole); Int = internal vibrations.

intermolecular bonds in 17α-hydroxyprogesterone crystals is 19.78 kcal mol^{-1}, which considerably exceeds the crystal packing energy in progesterone (9.67 kcal mol^{-1}) [31].

Thus, even when a crystal retains both long-range order in the arrangement of its molecules and its spatial symmetry, its THz absorption spectrum is very sensitive to slight changes in the structure of the molecules and to the presence of intermolecular hydrogen bonds. The results obtained to date demonstrate that there is a one-to-one correspondence between the topology of the absorption spectra of the steroid hormone molecules under consideration and their structure.

Owing to their structure, the steroid hormones have similar UV absorption spectra, with a peak at a wavelength of 240 nm, due to the presence of a conjugated ketone group in the A ring, which makes it impossible to analyse a mixture of steroid hormones. Conventional IR spectroscopy also has not found wide application in analysis of steroid hormones because of its low sensitivity [32]. As shown earlier [33–36], corticosteroid hormones have several strong characteristic absorption lines in the THz frequency range, which allow individual substances to be identified with certainty (Fig. 10).

Our data on the absorption spectra of a wide range of steroid hormones are summarised in Table 1. To analyse a steroid

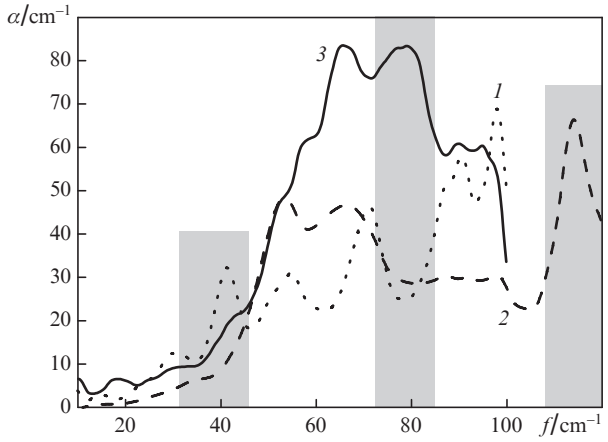

Figure 10. Absorption spectra of (*1*) progesterone, (*2*) 17α-hydroxyprogesterone and (*3*) cortisone. The rectangles indicate the frequency ranges that can be used for the identification of these substances in mixtures.

Table 1. Positions of resonances in the THz absorption spectra of steroid hormones.

Class	Substance	Frequency/THz
Progestins	Progesterone	0.89, 1.24, 1.68
	17α-Hydroxyprogesterone	1.57, 2.01
Gluco-corticoids	Cortisol	1.29, 2.71
	Cortisone	1.94, 2.43
	11-Deoxycortisol	1.51, 2.28, 3.39
Mineralo-corticoids	Corticosterone	1.59, 1.95, 2.56
	Deoxycorticosterone	1.45, 1.97
	Aldosterone	1.27, 1.78
Androgens	Dehydroepiandrosterone	1.39, 1.95
	Androstenedione	1.15, 1.88, 2.42
	Testosterone	1.42, 1.88, 2.40
	5α-Dihydrotestosterone	1.09, 1.45, 2.39
Estrogens	Estradiol	2.29, 2.68
	Estrone	1.27, 1.45, 1.74, 2.51
	Estriol	1.31, 1.74, 2.23, 2.83
Medicines	Cortisone acetate	1.57, 1.82
	Cortisol acetate	1.55, 2.17
	Corticosterone acetate	1.73, 2.17, 2.49, 2.94
	Deoxycorticosterone acetate	1.32, 2.25

mixture, it is possible to find characteristic frequencies suitable for hormone determination in complex matrices, which opens up the possibility of utilising terahertz time-domain spectroscopy in analyses of medicines and food for steroid hormones, as well as in pharmacological and chemical syntheses.

The THz absorption spectra of polycrystalline sugars contain both similar absorption lines (in the ranges 1.6–1.9 and 2.6–2.89 THz) and characteristic lines (Fig. 11a). With increasing frequency, the number of lines and the nonresonant background absorption typically increase. The lowest frequency line can be thought of as a characteristic one. For each type of sugar, this line has its own frequency: 0.54 THz for lactose, 1.44 THz for glucose monohydrate, 1.48 THz for arabinose, 1.72 THz for fructose, 1.82 THz for glucose and 1.83 THz for sucrose. Therefore, one can determine the percentages of individual components in a mixture of substances if the spectra of the components are known.

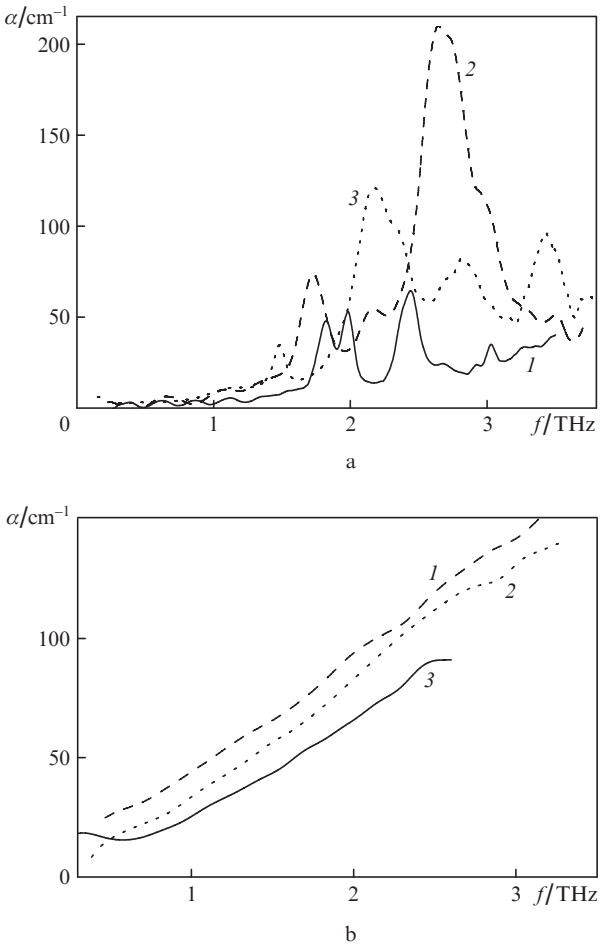

Figure 11. Absorption spectra of (a) (*1*) glucose, (*2*) fructose, (*3*) arabinose, (b) (*1*) DNA, (*2*) albumin and (*3*) haemoglobin.

Proteins and nucleic acids consist of a large number of elements and have several levels of structural organisation. The THz frequency range contains a high density of optically active modes. Because of the overlap of lines in spectra of dry preparations, characteristic lines cannot be separated out, as seen in the spectra of albumin, haemoglobin and high molecular weight DNA in Fig. 11b [17, 37].

3.2. Experimental studies of solutions and biological fluids using pulsed THz radiation

Our and other researchers' results demonstrate that, when crystalline substances having strong absorption bands in the THz frequency range are dissolved, the absorption spectra of the solutions have no sharp individual lines [30]. A transition from a polycrystalline substance to solution involves structural disordering, which leads to an increase in the density of vibrational states and broadening of individual vibrational resonances. In studies of solutions by THz spectroscopy, information about changes in the amplitude and shape of the spectrum is useful. The determination of these parameters is, however, often dependent on the measurement procedure and requires that the measurement reproducibility be carefully verified and that new, stable methods be developed [38].

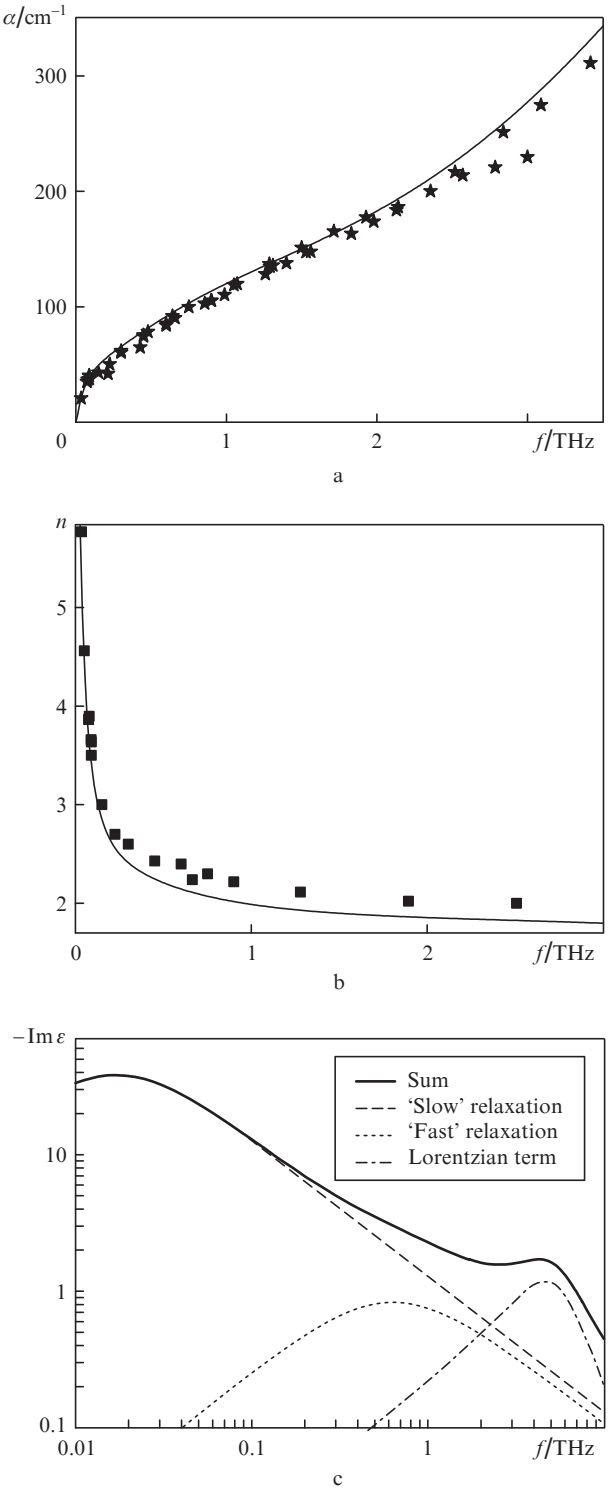

Figure 12. (a) Absorption and (b) refraction spectra of water and (c) components of the imaginary part of the dielectric function. The data points represent measurement results and the curves represent simulation results.

Changes in the shape of the spectrum are due to changes in the relaxation time of those liquid (water) molecules chemically or physically bound to the molecules of interest.

The dielectric permittivity of water was presented in the literature [39] and can be described by a two-component Debye model and a Lorentz term:

$$\varepsilon(\omega) = \varepsilon_\infty + \frac{\varepsilon_s - \varepsilon_1}{1 + i\omega\tau_D} + \frac{\varepsilon_1 - \varepsilon_\infty}{1 + i\omega\tau_2} + \frac{A}{\omega_0^2 - \omega^2 + i\omega\Gamma}, \quad (11)$$

where $\tau_D = 9.36$ ps and $\tau_2 = 0.3$ ps are the response times of the first ('slow') and second ('fast') Debye terms; $\varepsilon_\infty = 2.5$ is high-frequency permittivity; $\varepsilon_s = 80.2$ and $\varepsilon_1 = 5.3$ are the contributions of the first and second Debye terms to low-frequency permittivity; and $A = 38$ (THz/2π)^2, $\omega_0 = 5.6$ THz/2π and $\Gamma = 5.9$ THz are the amplitude, frequency and full width at half maximum of a Lorentzian line (Fig. 12c). In Fig. 12, the spectrum of liquid water calculated using Eqn (11) is compared to measured absorption and refraction spectra.

Liquid water strongly absorbs THz radiation: a 200-μm-thick water layer attenuates a THz field at a frequency of 1 THz by an order of magnitude, and a 1-mm-thick layer is essentially opaque over the entire THz range [40]. In the case of a relatively weak absorption, the highest sensitivity to changes in the composition of aqueous solutions is expected in the range 0.05–1.0 THz, so a THz generator and detector optimised for this range are needed. Since water strongly absorbs THz radiation, it is necessary to optimise the water layer thickness for measurements in transmission geometry. The most reproducible and informative measurements in the range 0.05–1.0 THz were made at a water layer thickness of 200 μm, which ensured transmittances in the range 0.2–0.5 and a signal-to-noise ratio of 10.

The blood components differ markedly in water content. For example, blood plasma contains more than 90% water, whereas the water content of the red blood cells is about 65%. The absorption coefficient of the red blood cells is smaller than that of water (Fig. 13a). The difference is 12% to 19% at concentrations of 5.7×10^6 to 7.32×10^6 cells per millilitre, respectively. According to experimental data, the absorption coefficient of the red blood cells is a linear function of their concentration at frequencies of 0.5, 1.0 and 1.5 THz.

As shown in our studies of absorption spectra of blood plasma, the absorption spectra of the blood plasma of healthy animals differ little in shape and amplitude from those of water (Fig. 13b). At the same time, the absorption spectrum of the blood plasma of a rat with experimental diabetes (glucose level as high as 30 mmol L^{-1}) has a smaller amplitude, as does the spectrum of a glucose solution (55.5 mmol L^{-1}). Animals with aloxan-induced diabetes differed significantly in the steroid hormone level in their blood from healthy rats [41]. Thus, the distinctions observed in the absorption spectra of liquids in the THz range are due in many respects to the fact that some of the water molecules, which strongly absorb THz radiation, are replaced by solute molecules, which leads to a decrease in water concentration.

In studies of solutions and biological samples, ATR spectroscopy proves to be more effective in a number of instances because it is more sensitive to small distinctions between spectra of solutions in the THz range than are transmission measurements in a cuvette. Since water and aqueous solutions strongly absorb THz radiation, in spectroscopic studies it is more convenient to employ not the signal transmitted through a liquid layer but the signal reflected from its surface. In the ATR technique, the dielectric permittivity is evaluated from the spectrum of the THz signal reflected from the interface between a silicon prism and the liquid of interest. Formulas for analysis of ATR spectra are presented in the preceding section.

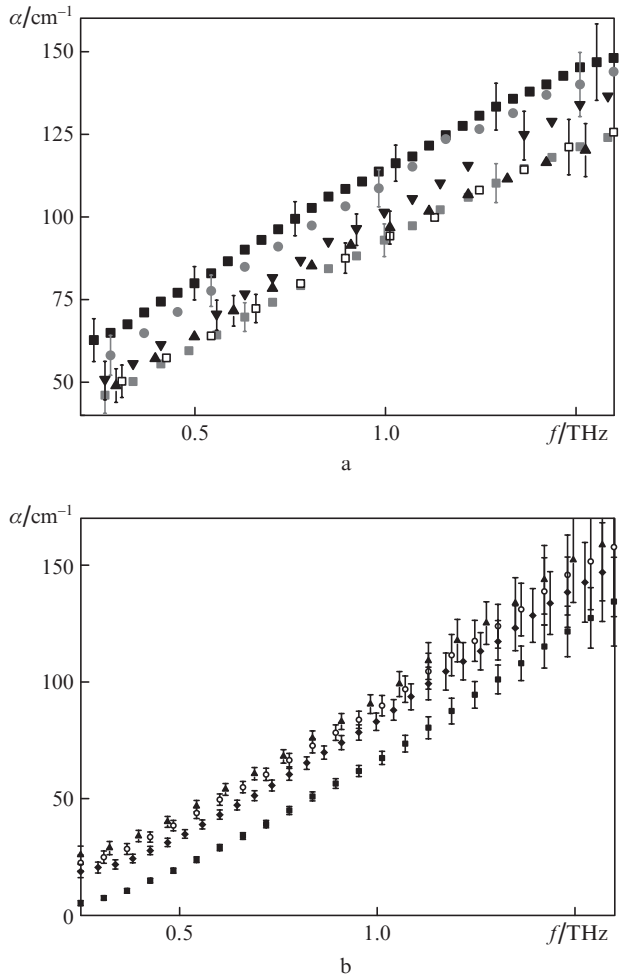

Figure 13. (a) Absorption spectra of water (■), blood plasma (●) and red blood cells (▼, ▲, □, ■) in human blood at red blood cell concentrations from 5.7×10^6 (▼) to 7.32×10^6 (■) cells per millilitre and (b) absorption spectra of water (▲), the blood plasma of a control rat (○) and a rat with diabetes (◆) and a glucose solution (■).

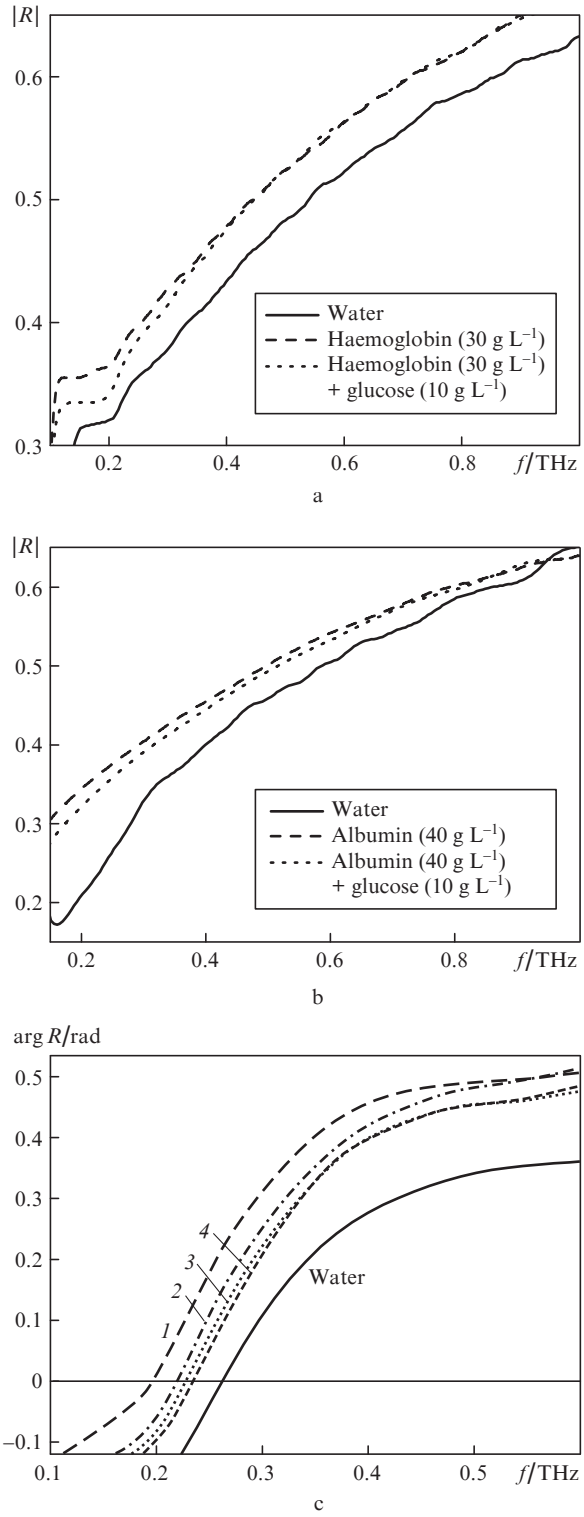

Figure 14. Reflection spectra of (a) haemoglobin and (b) albumin solutions and their mixtures with a glucose solution, and (c) phase of the reflection coefficient of aqueous lactose solutions at concentrations from (*1*) 25 wt% to (*4*) 3 wt%.

In ATR studies of aqueous protein and sugar solutions (Fig. 14), we observed the following general trends: the amplitude spectrum shifts upwards and the phase spectrum shifts to higher frequencies.

From the reflection amplitude in the range 0.2–2.0 THz, one can reliably determine the weight fraction of solutes in water in the range 2% to 6%. From the phase (of the reflection spectrum), one can reliably determine solute concentrations down to 3%. In the range 0.2–0.35 THz, improvement to 1% is possible: here the phase intersects the abscissa, and the curves for water containing an impurity lie to the left of those for pure water (Fig. 14c). The reflection spectrum of the protein is featureless in this spectral range. Water absorbs THz radiation several times more strongly than does the dry protein, and the dispersion of the refractive index of water is considerably higher. Changes in the shape of a spectrum may characterise the solute, as was observed for protein and DNA dissolution in water [37], but characteristics of the solute are difficult to assess from such changes at low solution concentrations.

Measurements of the transmission spectrum of solutions in a cuvette make it possible to more accurately determine the properties of the solution at frequencies below 0.3 THz. The prism in ATR geometry offers the possibility to measure a broader spectrum (at frequencies above 1 THz). Both methods can be used to determine τ_D, and only the configuration with a prism is suitable for assessing τ_2. The measurement procedure with a cuvette is less stable in terms of liquid layer thick-

ness reproducibility from sample to sample, which leads to a shift of refraction spectra and the imaginary part of the permittivity along the vertical axis. The configuration with a prism is more sensitive to a small time delay between the signal from the solution and the reference signal, which leads to different slopes of the reflection phase spectrum.

3.3. Experimental studies of biological tissues

In studies of a number of biological tissues in the frequency range under consideration, Nazarov et al. [17] obtained large absorption coefficients comparable in magnitude, whereas the refractive indices of the tissues differed markedly. This feature makes it possible to measure the amplitude of pulses reflected from interfaces between different layers of a tissue provided there is a considerable increase in signal-to-noise ratio in the pulsed THz spectrometer.

The absorption (and refraction) spectra of the tissues studied are similar in shape. This is due in part to the presence of water in the tissues [39] (the spectrum of water is similar in shape to that of the tissue, but its absorption coefficient is several times larger). Moreover, the spectra of biological macromolecules also have a similar shape (linear or quadratic increase in absorption coefficient and decrease in refractive index with increasing frequency). One possible explanation for why dry tissues have no characteristic lines is as follows: the spectra of biomolecules contain many lines, especially at high frequencies, where the lines overlap to form a continuum. A more in-depth study is needed, however, to address this issue in detail.

Two questions are of fundamental importance in studies of biological tissues and relate to the probing depth and the layered structure of the medium. The proposed measurement technique provides information only about the interface between media (the effective depth where the reflected signal is formed is tens of microns). In studies of layered media, pulses reflected from different surfaces can be separated in time if the layers are ~100 μm in thickness. One can then apply Fresnel's formula to each layer with its own reflection coefficient and three-dimensional parameters of the medium (layer) between the surfaces, which is traversed twice by the radiation. In the visible spectral region, such a technique was developed, e.g., for a three-layer skin model [42], and it can be adapted to the THz range.

4. THz imaging: from basic principles to typical applications

THz imaging of an object is of interest for a number of applications related to the detection and localisation of particular substances in an object under study. The fact that many organic substances have strong absorption bands in the THz range allows one to detect and identify such substances using THz spectroscopy and imaging. In optical image analysis, use is often made of 'pseudocolour' images in which low pixel brightness is represented by blue and high brightness is represented by red, or vice versa. Generally, this approach offers the possibility to improve image perception, but it has a number of limitations when one needs to identify a substance using an image of an object: the result depends significantly on illumination conditions, and a low spectral contrast in samples containing several substances of interest impedes the identification of substances having similar or overlapping spectra.

One way to improve image informativeness is to increase the number of channels (layers) in which images are acquired in the spectral selection of images through illumination or in the detection process. Multispectral laser imaging combines narrow-band illumination strictly corresponding to the spectral features of an object and standard (passive) image acquisition methods and can be used to collect an image of an object and identify substances of interest from their spectral signatures. For example, Brydegaard et al. [43] described a system in which an object could be illuminated using 13 independent light sources. Spectral discrimination in this system is ensured by sequentially turning on each source. Combining images in various spectral ranges makes it possible to significantly improve the clarity of images acquired using such a multichannel system. Practical application of a multichannel image acquisition system was described by Clancy et al. [44], who utilised multispectral imaging of a large intestine during a surgical procedure: multiple images were used to monitor the relative haemoglobin concentration in the tissue. In addition, they demonstrated the possibility of monitoring the arterial blood content of tissues during surgery.

Watanabe et al. [45] proposed taking into account spectral information in acquiring THz images for nondestructive chemical analysis of an object. They substantiated a method for analysis of multispectral THz images in which each point contained the transmission spectrum of the object. The method was implemented in the spectral range 1–2 THz and involved the use of known THz absorption spectra of the substances to be detected. The method was developed further by Shen et al. [46], who obtained THz images using broadband THz pulses (0.06–4.0 THz) reflected from the object of interest. If the characteristics of an object are unknown, it is necessary first to reveal inhomogeneities in its image and then, using image phase analysis results, to turn to a 'targeted' examination of the region of interest. For example, to acquire a THz image Shen et al. [46] used broadband illumination which had up to 60 independent spectral channels at a working bandwidth of ~3 THz and spectral resolution of 50 GHz. This made it possible to select images of various substances if these had spectral features in the indicated working range. Note that knowledge of the absorption spectra of the substances present in an object was unnecessary.

In this study, we propose further development of this approach, based on the concepts of multispectral and multitemporal domains, which combine the principles of colour vision, phase analysis and tomography in THz image acquisition, and describe application of the proposed technique.

4.1. Experimental apparatus and samples for THz imaging

To obtain THz images, use is made of a TPS Spectra 3000 pulsed THz spectrometer (TeraView Ltd) equipped with a reflection imaging module [47]. This configuration is used to detect pulsed THz radiation (0.06–4.0 THz) reflected from an object secured to a motor-driven xy translation stage, which ensures scanning in a horizontal plane over an area up to 80×80 mm in dimensions. The data thus obtained have the form of a three-dimensional (3D) array of $E(x_i, y_j, t_k)$ values, each of which is proportional to the amplitude of the electric field of the THz wave that came from the point at x_i and y_j on the sample surface at time t_k. Standard software supplied with the spectrometer allows one not only to analyse measured 3D arrays/images for each individual point (x_i, y_j)

by examining the temporal profile $E(t)$ of the reflected signal or its Fourier spectrum $E(f)$ but also to map out sections through an image: a time-domain section at a particular instant in time or a spectral section at a particular frequency. A point-by-point analysis of the spectrum of the reflected signal makes it possible to determine the chemical composition at each point of the sample, and analysis of the temporal profile provides information about the homogeneity of the sample and the magnitude of internal inhomogeneities. If a spectral feature characteristic of the substance of interest is found in the spectrum of the reflected signal, a spectral section at some characteristic frequency allows one to visualise the spatial distribution of the substance over the entire image obtained.

Thus, in addition to a point-by-point analysis of a sample, one can map out a time-domain or frequency-domain section through its image, i.e. to carry out layer-by-layer analysis in the frequency or time domain. It is worth pointing out that, in the case of a point-by-point analysis of an image, spectral analysis cannot be carried out simultaneously over the entire image. A layer-by-layer analysis of spectral sections through an image at a particular frequency, in turn, offers the possibility to visualise the presence and spatial distribution of a substance that has a spectral feature at that frequency, which makes it impossible to simultaneously detect and visualise several distinct substances. Also, analysis of a time-domain section is incapable of simultaneously visualising inhomogeneities located at different depths with respect to the sample surface. To overcome these limitations, we proposed and tested the concepts of multispectral and multitemporal domains in THz imaging. The use of these concepts allowed us to improve image contrast and considerably reduce the time needed to detect and localise substances of interest and hidden objects. To test the proposed concept, we prepared and studied the following samples:

(1) arabinose, lactose and hydroperit powders packed in polyethylene bags;

(2) sandwich structure in the form of three metallic discs located on different cardboard layers; and

(3) biological tissue in the form of a human skin sample affected by basal cell carcinoma.

4.2. Multiband THz imaging in the spectral domain

The concept of multispectral domain in THz imaging is based on a continuous layer-by-layer summation of spectral sections through an image and a superposition of specially designed digital spectral filters, whose position is determined with allowance for characteristic features in the reflection spectra of the substances of interest. Figure 15 illustrates the multispectral approach in THz imaging and its results by the example of acquiring THz images of arabinose, lactose and hydroperit powders packed in polyethylene bags. These substances cannot be distinguished in the photographs of the bags with the powders in Fig. 15b. The THz spectra of the signal reflected from the powders and the positions of three digital filters (red, R; green, G; and blue, B) with Gaussian profiles are shown in Fig. 15a. For each filter, the integral $Y_i^{(j)} = \int E_i(f) F_j(f)\,\mathrm{d}f$, where $E_i(f)$ is the spectrum of the THz pulse at the ith point of the image and $F_j(f)$ is the jth digital filter ($j = 1, 2, 3$ in the case represented in Fig. 15) is calculated point by point, and three numbers (R_i, G_i and B_i), corresponding to the red, green and blue colour components, are assigned to each pixel of the image. A THz image acquired in the multispectral domain is presented in Fig. 15c, where the three substances are easy to distinguish. It is worth pointing out that the presence of interference oscillations in the spectra in Fig. 15a and the nonuniform coloration of the homogeneous substance in Fig. 15c are caused by the influence of the packaging and the nonuniform thickness of the layers of the substance in the bags.

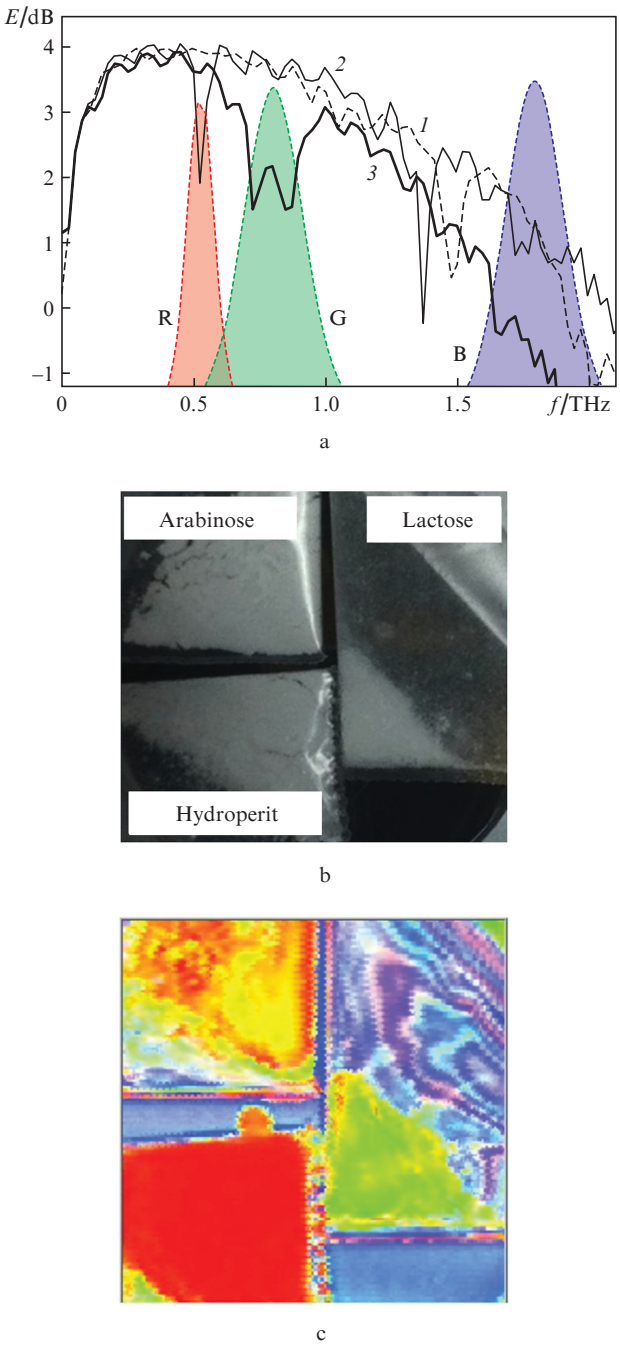

Figure 15. Multispectral domain in THz imaging: (a) THz reflection spectra of (*1*) arabinose, (*2*) lactose and (*3*) hydroperit powders packed in polyethylene bags and digital spectral filters with Gaussian profiles; (b) photographs of the bags with the powders; (c) THz image acquired in the multispectral domain. A colour version of this figure (along with those of Figs 16 and 17) is available online at http://www.quantum-electron.ru.

Note that, in the case of 24-bit colour images, the numbers R_i, G_i, and B_i should be normalised. We considered the following schemes for performing the normalisation procedure:

1. At each ith point of the image, we find the maximum and minimum colour components: $\max(R_i, G_i, B_i)$ and $\min(R_i, G_i, B_i)$. The normalised value of the jth colour component at the ith point, $\overline{Y_i^{(j)}}$, is calculated from its unnormalised value $Y_i^{(j)}$ as follows:

$$\overline{Y_i^{(j)}} = \frac{Y_i^{(j)} - \min(R_i, G_i, B_i)}{\max(R_i, G_i, B_i) - \min(R_i, G_i, B_i)} \times 256.$$

This point-by-point normalisation scheme allows one to extend the dynamic range of the colour image, enhance the colour depth, increase the number of colour hues and visually distinguish more details in the image.

2. As distinct from the above scheme, global normalisation is performed, i.e. the global extrema over the image, $\max(R, G, B)$ and $\min(R, G, B)$, are used for normalisation, instead of the point-by-point maxima and minima of the colour components. This normalisation scheme allows one to more effectively solve the problem of phase analysis when seeking uniform inclusions against an unknown background, where the visualisation of their specific details in images is not very important.

Thus, an appropriate scheme is chosen for performing the normalisation procedure, depending on the imaging purpose, and each pixel of the image is assigned a particular colour, depending on the spectral features of the substance at this point.

It is worth noting that, in general, the position, width and shape (rectangular, Gaussian or another) of filters are chosen arbitrarily. To effectively detect and localise substances of interest, it is reasonable to place filters in spectral regions with the most prominent features, because this leads to an increase in contrast and ensures a difference in colour and hue between the substances to be detected. An optimal choice of the set of digital filters allows one to visualise the presence of spectroscopically different substances in a sample.

4.3. Multiband THz imaging in the temporal domain

The concept of multitemporal domain in THz imaging is an analogue of the concept of multispectral domain and is based on a continuous layer-by-layer summation of time-domain sections through an image and a superposition of specially designed digital time-domain filters. The technique described above was used to analyse the temporal profile of a THz signal reflected from an object with a layered structure schematised in Fig. 16 a. Figure 16b shows the temporal profile measured at a point for a THz pulse reflected from such a structure. It consists of a series of successive (time-resolved) pulses corresponding to reflections from different cardboard layers. Also represented in Fig. 16b are the digital filters that were used for multitemporal THz imaging (Fig. 16c). In Fig. 16c, images of three objects are clearly seen. Their colours are straightforwardly determined by their depths in the sandwich, which offers the possibility to assess the spatial structure of the system.

4.4. Multiband THz imaging in the spectral and temporal domains for early skin cancer diagnosis

To conclude Section 4, we present multispectral and multitemporal THz imaging results for studies of biological tissue,

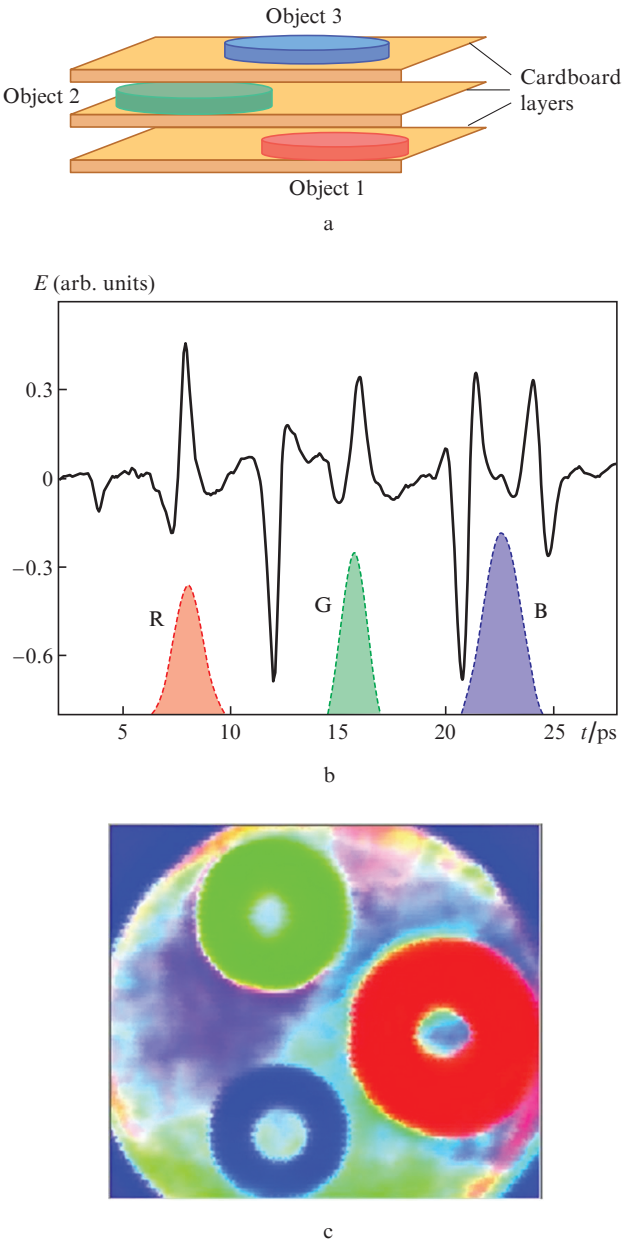

Figure 16. Multitemporal domain in THz imaging: (a) schematic of a sandwich structure (three metallic discs located on cardboard layers); (b) temporal profile of a THz pulse reflected from the sandwich structure and digital filters; (c) THz image acquired in the multitemporal domain.

illustrated by the example of the diagnosis of a human skin sample for skin cancer detection (Fig. 17). To detect skin lesion and localise the lesion focus, we used histological examination results (Fig. 17a). In Fig. 17a, the skin area affected by cancer is clearly seen. Figures 17b and 17c are multitemporal and multispectral THz images of the skin sample.

It is worth noting that the ability to detect basal cell carcinoma using reflection spectra of broadband THz pulses depends significantly on the surrounding tissues and the position of the tumour. Most of the techniques proposed to date analyse the temporal shape of a reflected pulse rather than its spectrum. Since a THz pulse broadens when reflected from an affected region in comparison with that reflected from healthy tissue, using specially adjusted time-domain digital filters one can

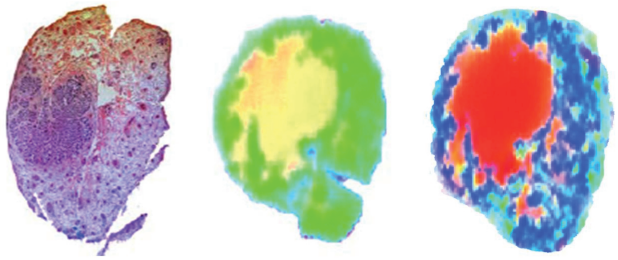

a b c

Figure 17. Images of a human skin sample affected by basal cell carcinoma: (a) histological cross section and (b) multitemporal and (c) multispectral THz images.

ensure a clear distinction between images of healthy and affected tissues (Fig. 17b).

Thus, in this study we have proposed and tested the concepts of multispectral and multitemporal domains in THz imaging with the aim of improving image contrast for the detection and localisation of substances of interest and hidden objects. We have demonstrated the effectiveness of multispectral and multitemporal THz imaging of solid and loose materials, sandwich structures and biological tissue.

5. Application of pulsed THz radiation in analysis of dielectric properties of nanostructured systems

An experimental analysis of the interaction of THz radiation with nanomaterials is significantly impeded by their weak effect on the THz signal. If the dielectric permittivity of a nano-object has no resonance properties in the THz range and the nano-object has no metallic properties (i.e. the plasma frequency for free charge carriers in it is substantially lower than the frequencies of the THz range), its effect on the transmitted THz radiation is extremely weak. It is, therefore, necessary to produce a sufficiently high volume concentration of such nano-objects in some region of a sample or on its surface. It is important that the individual nano-objects be isolated from each other, because otherwise percolation effects begin to show up [48] and the system acquires properties of a continuous medium.

One approach to the study of nano-objects in the THz frequency range is to apply the nano-objects of interest to the surface of a highly porous material transparent in the THz range. Highly porous materials have a large specific surface area and allow for high concentrations of particles isolated from each other. One example of a highly porous transparent material is nanostructured aluminium oxyhydroxide (NAO).

NAO can be produced by the selective oxidation of aluminium on the surface of a liquid mercury layer containing dissolved aluminium or gallium in a humid atmosphere at temperatures from 20 to 70 °C [49]. Two unconventional methods have been proposed for NAO synthesis using mercury and gallium, which ensure identical properties of NAO samples: low density (0.02–0.04 g cm^{-3}), high porosity (~99%) and large specific surface area (250–350 m^2 g^{-1}). The surface of such materials is highly reactive and suitable for modification by both isolated nanoparticles and monolayer coating. The structure of NAO has the form of a 3D network of amorphous nanofibrils ~5 nm in diameter, with the general formula $Al_2O_3 \cdot nH_2O$, where n takes values from 1 to 3.6, depending on synthesis conditions. When NAO is annealed at temperatures from 100 to 1700 °C, the 3D network remains intact and the material retains high porosity, but the chemical composition of the fibrils changes towards a decrease in water content and the linear dimensions of the sample decrease isotropically (Fig. 18). Annealing at different temperatures for various lengths of time allows one to tune the physical parameters of macroscopic samples over wide ranges: density from 0.04 to 3 g cm^{-3}, porosity from 99.3% to 25% and specific surface area from 350 to 1 m^2 g^{-1}.

We used porous NAO materials as a highly porous model system to study the dielectric properties of water chemically bonded and adsorbed on NAO fibrils. The flexibility in controlling the stoichiometric composition of the fibrils (by varying the water content in them) allowed us to compare their properties at various transformation stages: from the as-prepared, amorphous material ($Al_2O_3 \cdot 3.6H_2O$) to the highest temperature crystalline phase α-Al_2O_3.

The properties of NAO were studied using a THz time-domain spectrometer in transmission geometry. Dividing the Fourier transform of the THz signal transmitted through

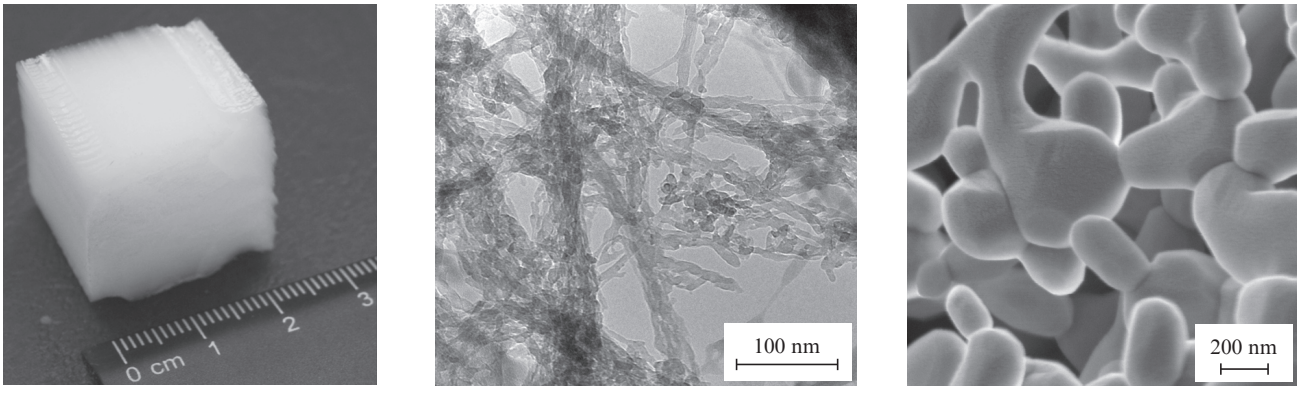

a b c

Figure 18. (a) As-grown NAO, (b) electron-microscopic image of fibrils in as-prepared NAO and (c) 3D network of fibrils after annealing for 4 h at a temperature of 1100 °C.

a porous sample by that of a reference signal obtained with no sample, one can evaluate the absorption coefficient and refractive index of the sample as a whole using Eqns (1).

The macroscopic characteristics of samples thus determined are, however, contributed not only by the dielectric permittivity of the NAO fibrils but also by the porosity of the material: in the as-prepared state, the sample contains up to 99 vol% air, whose dielectric permittivity is close to unity. Therefore, to go from the properties of a sample as a whole to those of individual fibrils, one should take into account how these fill the volume of the sample.

Clearly, the most direct way of taking into account the porosity of the medium – by exactly solving Maxwell's equations for the propagation of THz radiation through a particular porous sample – cannot be realised because of its extreme complexity and because it is impossible to provide an accurate morphological description of each sample in each processing step. A natural approach to this problem is to model the system by an effective isotropic medium. It is then thought that electromagnetic radiation 'sees' the sample as a uniform medium whose dielectric permittivity (and, hence, absorption coefficient and refractive index) depend on the dielectric permittivity of individual fibrils, the volume fraction of the fibrils in the sample (porosity), the geometry of the fibrils and their mutual orientation in the sample. Effective medium models typically rely on the electrostatic approximation, in which the particle size and the spacing between the particles are considerably smaller than the wavelength of electromagnetic radiation. In the case of THz radiation (wavelengths from 100 μm to 3 mm), this approximation is valid for NAO fibrils both before and after high-temperature annealing.

The simplest, and best known, effective medium models are the Maxwell Garnett, Bruggeman and Landau–Lifshitz–Looyenga models [50]. All these models neglect the actual shape of individual components of the effective medium, which is represented by an array of spheres. The first two models rely on a solution to the problem of the polarization induced by a dc electric field in a dielectric sphere with permittivity ε_1 in a dielectric medium with permittivity ε_2.

The Bruggeman model considers a medium composed of two equivalent components (air and fibril material) with permittivities ε_1 and ε_2 and fill factors f_1 и f_2, respectively. The fill factors are taken to meet $f_1 + f_2 = 1$. The dielectric permittivity of the entire medium, ε_{eff}, meets the relation

$$f_1 \frac{\varepsilon_1 - \varepsilon_{\text{eff}}}{\varepsilon_1 + 2\varepsilon_{\text{eff}}} + f_2 \frac{\varepsilon_2 - \varepsilon_{\text{eff}}}{\varepsilon_2 + 2\varepsilon_{\text{eff}}} = 0. \tag{12}$$

The applicability of this model is limited by the inequalities $^1/_3 < f_{1,2} < {}^2/_3$, i.e. the model is formally suitable only for samples with relatively high density, obtained e.g. by pressing NAO into pellets.

In the Maxwell Garnett model, a medium is thought of as a substance with permittivity ε_2 containing spheres (volume fraction f_1) with permittivity ε_1, and the entire composite is treated as an effective medium with permittivity ε_{eff}, surrounded by a substance with permittivity ε_2. In addition, the volume fraction f_1 of the spheres is taken to be small. In this approximation, the dielectric permittivity of the medium meets the relation

$$\frac{\varepsilon_{\text{eff}} - \varepsilon_2}{\varepsilon_{\text{eff}} + 2\varepsilon_2} = f_1 \frac{\varepsilon_1 - \varepsilon_2}{\varepsilon_1 + 2\varepsilon_2}. \tag{13}$$

Since the components of the effective medium are not equivalent, the Maxwell Garnett model can be applied to NAO in only two particular cases: a small amount of fibrils in an air matrix and air spheres in a fibril matrix.

In the Landau–Lifshitz–Looyenga model, the dielectric permittivity of the effective medium meets the relation

$$\varepsilon_{\text{eff}}^{1/3} = \langle \varepsilon^{1/3} \rangle. \tag{14}$$

Using the above models, we can determine the dielectric permittivity of NAO fibrils from the measured absorption and refraction spectra of samples by solving the inverse problem for each particular model. Indeed, measurements give us the absorption and refraction spectra of a sample as a whole. From such data, we extract the complex dielectric permittivity of the effective medium:

$$\varepsilon_{\text{eff}} = \varepsilon' + \mathrm{i}\varepsilon'', \tag{15}$$

where $\varepsilon' = n^2 - (\alpha c/\omega)^2$ and $\varepsilon'' = 2n(\alpha c/\omega)$. Further, using Eqns (12)–(14) and knowing the porosity of a particular sample, we can find the complex dielectric permittivity of the fibrils.

It is worth pointing out that, to determine the dielectric permittivity of the fibrils in the uncompacted samples, which had high porosity, we used the Maxwell Garnett model for air bubbles in a fibril matrix because, at high porosities, the other models lead to extremely overestimated values of the real part ε' for the fibrils and to a large scatter in the real part for samples prepared from the same piece of the material but compressed in the longitudinal direction to various densities. Thus, only this model proved to be stable to small variations in parameters in the porosity range examined. For samples pressed into pellets with a relatively high density (~60%), the Bruggeman model leads to results similar on the whole to those obtained in the Maxwell Garnett model.

Figure 19 shows typical spectra of the real and imaginary parts of the dielectric permittivity of NAO fibrils (exemplified by a sample annealed at a temperature of 650 °C for 4 h.

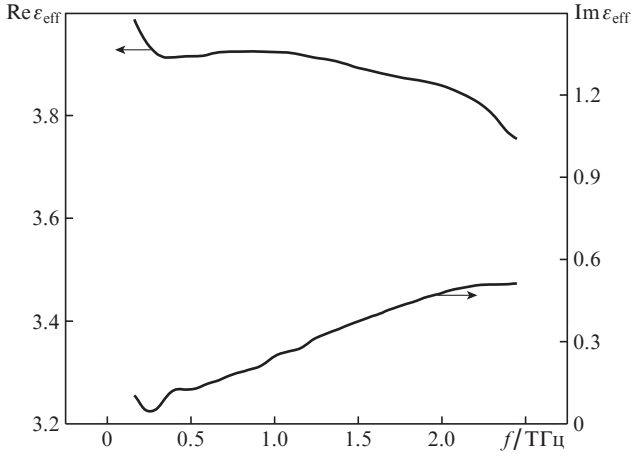

Figure 19. Typical dielectric permittivity spectra obtained for NAO fibrils in the Maxwell Garnett model. The sample was annealed at a temperature of 650 °C for 4 h.

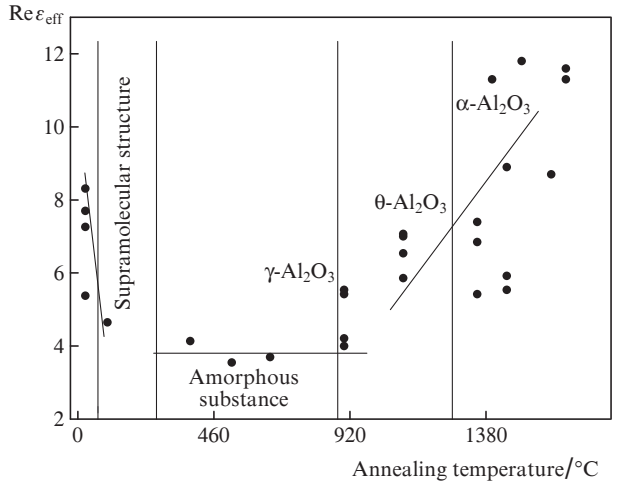

Figure 20. Effect of annealing temperature on the real part of the dielectric permittivity of NAO fibrils.

Using the Maxwell Garnett model, we can compare the dielectric permittivities of the NAO fibrils after annealing at temperatures from 100 to 1500 °C. As a comparison criterion, we use the real part of 1-THz permittivity. The calculated ε' values are presented in Fig. 20. It is seen that the evolution of the dielectric permittivity can be divided somewhat arbitrarily into several distinct portions: comparatively high ε' before annealing; a small slope below 700 °C, where ε' varies little; and a monotonic increase in ε' at high annealing temperatures (above 1000 °C). It is also worth noting that the dielectric permittivity of corundum (in the limit of zero porosity and high-temperature annealing, NAO is very similar to corundum) in the THz frequency range is ~9 [51].

According to the characterisation of the NAO fibrils by a number of physical techniques [X-ray diffraction, IR spectroscopy, thermogravimetric analysis (TGA), scanning and transmission electron microscopy and others), annealing at temperatures from 100 to 1500 °C causes NAO to undergo a number of structural phase transitions. The as-grown, unannealed fibrils have a complex supramolecular structure with high water content and a high density of hydrogen bonds, which stabilize the structure. Annealing at moderate temperatures (up to 440 °C) breaks down the supramolecular structure and removes most of the water (the structural composition changes from $Al_2O_3 \cdot 3.57H_2O$ to $Al_2O_3 \cdot 0.71H_2O$). The material becomes X-ray amorphous in this range of annealing temperatures. During further annealing, NAO sequentially transforms into three crystalline phases: γ-Al_2O_3 (at a temperature below 1000 °C), θ-Al_2O_3 (below 1100 °C) and α-Al_2O_3 (above 1100 °C). In this process, the water and OH content of the material gradually decreases to zero (Table 2, TGA data).

Table 2. Water content of NAO materials at different heat-treatment stages.

Annealing temperature/°C	Water molecules per Al_2O_3 molecule	Irreversible water loss at 930 °C	Reversible water adsorption
25 (without annealing)	3.57	2.85	0.72
75	2.18	1.46	0.72
100	1.45	0.73	0.72
380	0.88	0.16	0.72
400	0.71	0.16	0.55
520	0.58	0.096	0.48
660	0.623	0.038	0.585

Since we calculated the dielectric permittivity of the NAO fibrils using an effective medium model, thus taking into account changes in the macroscopic characteristics (density and porosity) of the samples, it is the annealing-induced changes in their structural and phase compositions that are responsible for all the changes in ε'. It is seen that, in an amorphous state (100–700 °C), the NAO fibrils have the lowest dielectric permittivity. After crystallization, the dielectric permittivity approaches a value characteristic of corundum. The sharp drop in permittivity at the lowest annealing temperatures is caused by water loss. In this process, the supramolecular structure breaks down and the fibrils become amorphous.

The effect of water on the THz permittivity of the material can be detected in another way. Since the NAO samples annealed at temperatures below 1000 °C have a large specific surface area and, hence, high adsorption capacity, there is a considerable amount of reversibly physisorbed water on their surface at room temperature (Table 2, last column). This

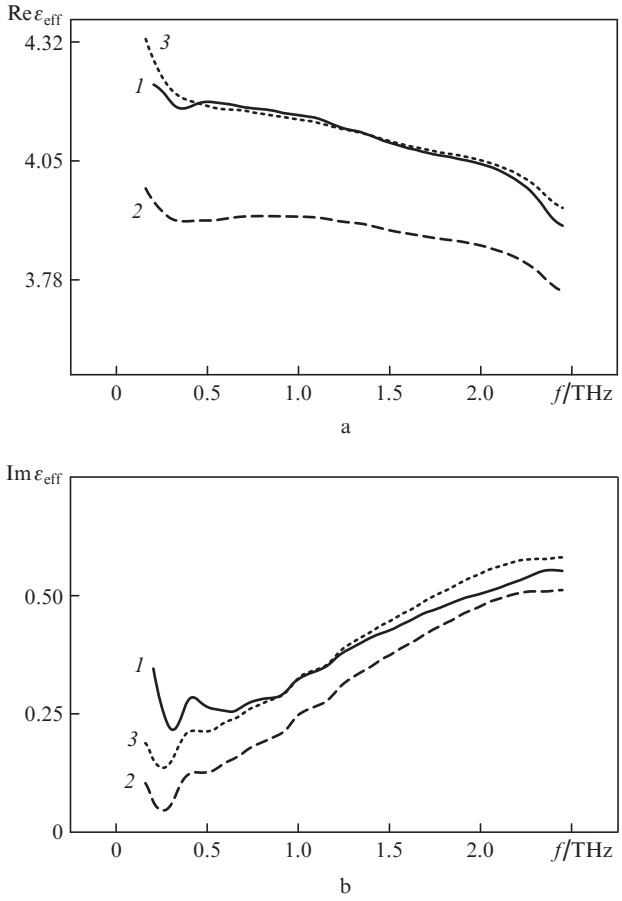

Figure 21. (a) Real and (b) imaginary parts of the dielectric permittivity of an NAO sample after (*1*) annealing at a temperature below 650 °C and (*2*) subsequent holding under vacuum; (*3*) dielectric permittivity calculated in the Maxwell Garnett model for a dry fibril + water composite containing 0.1 vol% water.

water can be partially removed, e.g. by holding the sample in vacuum. Figure 21 shows the spectra of the real and imaginary parts of the dielectric permittivity of an NAO sample after annealing at a temperature below 650 °C and after subsequent holding under vacuum (10^{-6} Torr). The observed change in permittivity is due to the partial removal of the adsorbed water from its surface.

To describe this change, we used the Maxwell Garnett model and represented a fibril at atmospheric pressure as a composite consisting of a 'dry fibril' material (in vacuum) and water. To this end, we used the THz permittivity of water reported by Nagai et al. [52]. Curve (*3*) in Fig. 21 shows the permittivity spectrum calculated in the Maxwell Garnett effective medium model for fibrils containing 0.1 vol% water.

Thus, the example of NAO indicates that THz spectroscopy can be used to study nano-objects. Experimental data demonstrate the feasibility of assessing the dielectric properties of nano-objects distributed over a sample. The method is shown to be sensitive to the composition of the material and the presence of thin layers of physisorbed molecules, such as water, on its surface.

6. Conclusions

More than two centuries have passed since Herschel's studies [3] and a hundred years will soon have passed since Glagolewa-Arkadiewa's research, but the 'terahertz community' is still at the beginning of the way to mature THz technology and many photonic and electronic devices have to be developed for the THz range. It is already clear that radiation in this frequency range can be used in medical, industrial and security applications. Independent of the development of techniques for the generation, detection and control of THz radiation, investigation of 'living' systems will always be its priority application area. Here, its diagnostic potentialities have been well studied and it has been shown to be highly informative.

Acknowledgements. We are grateful to V.V. Tuchin, A.N. Khodan, I. Garian, I.N. Smirnova and A. Yaroslavskaya who participated in some of the studies whose results are presented in this paper.

This work was supported by the Russian Foundation for Basic Research (Grant Nos 14-02-00979, 13-02-01364 and 12-08-00921).

References

1. Brüdermann E., Hübers H.-W., Kimmitt M.F. *Terahertz Techniques* (Heidelberg: Springer, 2011) p. 394.
2. Della Porta G. *Magia Naturalis Sive de Miraculis Rerum Naturalium* (1558).
3. Herschel W. *Philos. Trans. R. Soc. London*, **90**, 284 (1800).
4. Rubens H., Snow B.W. *Philos. Mag*., **35**, 35 (1893).
5. Geddes P. *The Life and Work of Sir Jagadis C.Bose* (London: Longmans, Green and Co., 1920) p. 56.
6. *Collected Physical Papers of Sir Jagadis C.Bose* (London–New York–Toronto–Bombay–Calcutta: Longmans, Green and Co., 1927) pp 374–397.
7. Glagolewa-Arkadiewa A. *Nature*, **113** (2844), 640 (1924).
8. Glagolewa-Arkadiewa A.A. *Usp. Fiz. Nauk*, **6** (3), 216 (1926).
9. Callahan P.S. *Fla. Entomol.*, **54** (2), 201 (1971).
10. Cheung K.P., Auston D.H. *Infrared Phys.*, **26** (1), 23 (1986).
11. Lee Y.-S. *Principles of Terahertz Science and Technology* (New York, USA: Springer Science+Business Media, 2009) p. 51.
12. Zhang X.-C., Xu J. *Introduction to THz Wave Photonics* (New York, USA: Springer Science+Business Media, 2010).
13. Schmuttermaer C.A. *Chem. Rev*., **104** (4), 1759 (2004).
14. Nazarov M.M., Shkurinov A.P., Angeluts A.A., Sapozhnikov D.A. *Izv. Vyssh. Uchebn. Zaved. Ser. Radiofiz*., **52**, 595 (2009) [*Radiophys. Quantum Electron*., **52**, 536 (2009)].
15. Angeluts A.A., Bezotosnyi V.V., Cheshev E.A., et al. *Laser Phys. Lett.*, **11**, 015004 (2014).
16. Borodin A.V., Esaulkov M.N., Kuritsyn I.I., et al. *J. Opt. Soc. Am. B*, **29** (8), 1911 (2012).
17. Nazarov M.M., Shkurinov A.P., Kuleshov E.A., Tuchin V.V. *Kvantovaya Elektron*., **38**, 647 (2008) [*Quantum Electron*., **38**, 647 (2008)].
18. Schaefer H., Redelmeier T.E. *Skin Barrier, Principles of Percutaneous Absorption* (Basel: Karger AG, 1996).
19. Safonov V.N., Trofimov V.A., Shkurinov A.P. *Zh. Tekh. Fiz*., **76** (4), 78 (2006) [*Tech. Phys*., **51** (4), 470 (2006)].
20. Nazarov M.M., Mukina L.S., Shuvaev A.V., et al. *Laser Phys. Lett.*, **2** (10), 471 (2005).
21. Kitaigorodskii A.I. *Molecular Crystals and Molecules* (London: Academic, 1973; Moscow: Nauka, 1971).
22. Xie A., Meer A.F.G., Austin R.H. *Phys. Rev. Lett*., **88** (1), 018102 (2002).
23. Laman N., Harsha S.S., Grischkowsky D., Melinger J.S. *Biophys. J*., **94**, 1010 (2008).
24. Borodin A.V., Gayvoronsky V.Ya., Kachkovsky O.D., et al. *Opt. Spektrosk.*, **107** (4), 505 (2009).
25. Smirnova I.N., Sapozhnikov D.A., Kargovsky A.V., et al. *Vibr. Spectrosc.*, **62**, 238 (2012).
26. Bürgi H.B. *Annu. Rev. Phys. Chem*., **51**, 275 (2000).
27. Walther M., Fischer B., Schall M., et al. *Chem. Phys. Lett.*, **332**, 389 (2000).
28. Minaeva V.A., Minaev B.F., Hovorun D.M. *Ukr. Khim. Zh.*, **80**, 82 (2008).
29. Minaeva V.A., Minaev B.F., Baryshnikov G.V., et al. *Vestn. Cherkassk. Univ. Ser. Khim. Nauki*, **195**, 25 (2011).
30. Smirnova I., Fedulova E., Nazarov M., Cherkasova O. *Vestn. Novosibirsk. Gos. Univ. Ser. Fiz*., **5** (4), 170 (2010).
31. Baryshnikov G.V., Tkachenko L.I., Minaeva V.A., et al. *Vestn. Cherkassk. Univ. Ser. Khim. Nauki*, **267**, 124 (2013).
32. Görög S. *Quantitative Analysis of Steroids* (New York: Elsevier, 1983; Moscow: Mir, 1985).
33. Cherkasova O., Nazarov M., Sapozhnikov D., et al. *Proc. SPIE Int. Soc. Opt. Eng.*, **7376**, 73760P (2010).
34. Cherkasova O.P., Nazarov M.M., Mankova A.A., Fedulova E.V., Shkurinov A.P., Volodin V.A., Minaeva V.A., Minaev B.F., Baryshnikov G.V. *Vestn. Cherkassk. Univ. Ser. Khim. Nauki*, **175**, 28 (2010).
35. Minaeva V.A., Cherkasova O., Khmara A.V. *Vestn. Cherkassk. Univ. Ser. Khim. Nauki*, **307**, 76 (2014).
36. Cherkasova O.P., Nazarov M.M., Smirnova I.N., Shkurinov A.P. *Proc. 20th Int. Conf. on Advanced Laser Technologies (ALT'12)* (Thun, Switzerland, 2012) pp 1–3; DOI: 10.12684/alt.1.86.
37. Cherkasova O.P., Nazarov M.M., Shkurinov A.P., Fedorov V.I. *Radiophys. Quantum Electron.*, **52** (7), 518 (2009).
38. Born B., Havenith M. *J. Infrared, Millimeter Terahertz Waves*, **30**, 1866 (2009).
39. Woods K.N., Wiedemann H. *J. Chem. Phys*., **123**, 134507 (2005).
40. Heugen U., Schwaab G., Bründermann E., et al. *Proc. Natl. Acad. Sci. U.S.A.*, **103**, 12301 (2006).
41. Cherkasova O.P., Selyatitskaya V.G. *Biochemistry (Moscow) Supplement. Ser. B: Biomedical Chemistry*, **7** (1), 90 (2013).
42. Dolotov L.E., Sinichkin Yu.P., Tuchin V.V., et al. *Lasers Surg. Med.*, **34**, 127 (2004).
43. Brydegaard M., Merdasa A., Jayaweera H., et al. *Rev. Sci. Instrum.*, **82**, 123106 (2011).

44. Clancy N.T., Stoyanov D., James D.R.C., et al. *Biomed. Opt. Express*, **3**, 2567 (2012).
45. Watanabe Y., Kawase K., Ikari T., et al. *Appl. Opt.*, **42**, 5744 (2003).
46. Shen Y.C., Lo T., Taday P.F., et al. *Appl. Phys. Lett.*, **86**, 241116 (2005).
47. http://www.teraview.com/products/terahertz-pulsed-spectra-3000/index.html.
48. Cooke D.G., Meldrum A., Jepsen P.U. *Appl. Phys. Lett.*, **101**, 211107 (2012).
49. Di Costanzo T., Fomkin A.A., Frappart C., Khodan A.N. *Mater. Sci. Forum*, **315**, 453 (2004).
50. Golovan' L.A., Timoshenko V.Yu., Kashkarov P.K. *Usp. Fiz. Nauk*, **177** (6), 619 (2007).
51. Gervais F. *Handbook of Optical Constants of Solids II* (San Diego, CA: Acad. Press, 1991) pp 761–775.
52. Nagai M., Yada H., Arikawa A., Tanaka K. *J. Infrared Millimeter Waves*, **27** (4), 505 (2006).